博士論文

論文題目　Cryo-Electron Microscopy Study of KIF and Microtubule Complex
(KIF-微小管複合体のクライオ電子顕微鏡構造解析)

氏　名　　森川　真夏

Contents

This work was published in the EMBO journal

(EMBO J. 2015 May 5;34(9):1270-86).

Acknowledgments

I would like to sincerely appreciate Prof. N. Hirokawa for his courteous instructions and encouragement for completing this project. I am also grateful to Drs. H. Yajima and R. Nitta for their scientific supervision; Drs. C. Sato and T. Ogura for image analysis; all the members of Hirokawa lab for helpful suggestions and discussion. This work was supported by the Ministry of Education, Culture, Sports, Science and Technology of Japan (MEXT), as a grant-in-Aid for Specially Promoted Research to N.H., and by grants to T.O. and C.S. from MEXT, the Japan New Energy and Industrial Development Organization (NEDO), and Japan Science and Technology Corporation (JST).

Abstract

The molecular motor kinesin moves along microtubules using energy from ATP hydrolysis. In neurons, kinesin-1/KIF5C preferentially binds to the GTP-state microtubules over GDP-state microtubules to selectively enter an axon among many neuronal processes. Although there have already been numerous papers reporting the structure of KIF and microtubule complex, initial step of KIF5C on GTP-state microtubule is unavailable and how KIF5C distinguishes the nucleotide state of microtubule remains poorly understood at the atomic level. Here, the cryo-electron microscopic structures of nucleotide-free KIF5C complexed with the GTP-state microtubule and GDP-state microtubule are presented. The structures illustrate mutual conformational changes induced by interaction between the GTP-state microtubule and KIF5C. Conformational changes to tubulin strengthen the longitudinal contacts of the GTP-state microtubule in a similar manner to GDP-taxol microtubules. On the GTP-state microtubule, KIF5C acquires the “rigor conformation”, where mobile switches I and II are stabilized through loop L11 and the initial portion of the neck-linker, facilitating effective ADP release. Functional analyses of KIF5C suggest that the binding between charged hydrophobic residues of L11 and the specific surface structure of

the GTP-state microtubule accomplishes a higher specificity than GDP-state microtubule. Collectively, our findings explain preferential binding of KIF5C to the GTP-state microtubule, and the polarized transport by KIF5C to the axon over the dendrites.

Introduction

Kinesin superfamily proteins (KIFs) are microtubule (MT)-based molecular motors that play fundamental roles in intracellular transport. Kinesins use energy from ATP to move along the MTs (Hirokawa et al., 2009a; Hirokawa et al., 2009b). Structural studies of kinesin motility have suggested that the energy generated by the hydrolysis of ATP is used for the active detachment from the MT track, whereas the energy produced by the binding to the MT, coupled with ADP release, allows the plus-end directed movement (Hirose et al., 2006; Kikkawa and Hirokawa, 2006; Kikkawa et al., 2001; Kozielski et al., 1997; Kull et al., 1996; Nitta et al., 2004; Nitta et al., 2008; Sablin et al., 1998; Sindelar and Downing, 2010). Based on this alternating attachment and detachment of a kinesin catalytic head, the hand-over-hand model has been proposed to explain the processive, cooperative movement of dimeric kinesin. According to this model, the two catalytic heads alternately "step" so that kinesin is always attached to the MT (Asbury et al., 2003; Block et al., 1990; Yildiz et al., 2004). This means that one head cannot hydrolyze ATP to detach from the MT until the other head has released ADP to attach strongly to the MT (Alonso et al., 2007). Hence, the mechanical process in which the catalytic head attaches to the MT, coupled with ADP release, defines the

coordination between the two heads.

The catalytic head of kinesin contains three conserved mobile regions switch I, switch II and a short strand "neck-linker", which undergo major conformational changes through the ATPase cycle (Kull et al., 1996). Switch I is the ATP hydrolysis catalytic region consists of helix α3, the following loop L9, and the phosphate-binding loop (P-loop). The P-loop and L9 form the right and left walls of the nucleotide-binding pocket. Switch II is a microtubule-binding region, containing a series of elements: loop L11, helix α4 and loop L12. The conformational change of switch II is explained by the rotation and the length of helix α4, with the elongation and extraction of the loops L11 and L12. The neck-linker links two catalytic heads and cargo in kinesin dimers. Switch I and switch II are connected by salt bridges which rearrange according to the nucleotide in the nucleotide binding pocket, inducing mechanical movement of kinesin dimer via neck-linker (Hirokawa et al., 2009a; Nitta et al., 2004).

MT is a helical architecture composed of αβ-tubulin hetero-dimer aggregating laterally into the protofilament. α-tubulin and β-tubulin share ~40% homology in sequence and are similar

in second structure (Nogales et al., 1998). GTP is necessary for α-tubulin and β-tubulin to polymerize into MT, but only the GTP in β-tubulin will be hydrolyzed. Therefore, within the dynamic MT, α-tubulin contains GTP and β-tubulin contains GDP (GDP-MT), while within the polymerization tip, both α- and β-tubulin contain GTP (GTP-MT).

To elucidate the molecular mechanisms of the fundamental processive movement of kinesin on MT, kinesin structures before and after ADP release, i.e., the Mg-ADP state and the nucleotide-free state, are necessary. Cryo-EM structure of nucleotide-free kinesin complexed with taxol-stabilized GDP-MT (GDP-taxol-MT) was reported for some types of kinesins, KIF5 (kinesin-1/conventional kinesin) and Kar3 (kinesin-14) (Atherton et al., 2014; Hirose et al., 2006; Sindelar and Downing, 2007). Both forms, however, take very different conformations, especially at the switch II element. The switch II conformation of KIF5 is similar to the crystal structure in the Mg-ADP state (ADP-like conformation), whereas the interface of Kar3 differs from both the Mg-ATP form (ATP-like conformation) and the ADP-like conformation. The reason for the difference between KIF5 and Kar3 is still debated and the high-resolution structure remains elusive.

Understanding this key mechanical step in KIF5 motility on MT has attracted the attention of cell biologists and neuroscientists. In neurons, KIF5 transports several types of cargo to the axon, not to the dendrites (Jacobson et al., 2006; Nakata and Hirokawa, 2003). This polarized transport in neurons is possible because, in axons, GTP-MTs are enriched over GDP-MTs and are preferentially "searched for" as landmarks by KIF5 (Nakata et al., 2011). This high-affinity binding of KIF5 to GTP-MTs guides various cargoes to their correct neuronal destinations. Recently, the structure of GTP-MT was reported and the characteristic feature of KIF5 binding site was suggested to account for the different affinity between KIF5 and GDP-/GTP-MTs (Yajima et al., 2012). To further understand the molecular mechanism of the fundamental relationship between kinesins and MTs, elucidation of the structures of KIF5 at the beginning of stepping, at the nucleotide-free state and complexed with GTP-MT, is necessary.

Here I describe the successful cryo-EM structure of nucleotide-free KIF5C complexed with GTP-state MT at 8.9 Å resolution. GTP-state MT was stabilized using GTP analog guanylyl 5'-a, b-methylenediphosphonate (GMPCPP). This analog promotes the polymerization of normal microtubules with the same polymerization rate to GTP, while the depolymerization

rate is extremely slow, so that GMPCPP-MTs are mimic of GTP-state MTs (Hyman et al., 1992). In silico docking of crystal structures with the cryo-EM structure revealed the mutual conformational changes of KIF5C and GMPCPP-MT. Nucleotide-free KIF5C complexes with GMPCPP-MT acquires a new conformation that I termed the “rigor conformation”, by analogy with myosin. This conformation not only provides an important missing link in the structural analysis of kinesin, but also elucidates the molecular mechanism of the preferential binding to the GTP-MT. Furthermore, this is the first observation of the conformational change in the GMPCPP-MT induced by KIF5C binding. GMPCPP-MT predominantly changes its surface conformation of α- and β-tubulins with strengthening of the longitudinal contacts. These structural and functional analyses provide the molecular mechanism of the preferential binding of KIF5 to GTP-state microtubules.

Results

GMPCPP-MT is a Better Substrate for KIF5C than GDP-MT

The binding of KIF5C to GTP-MT is 3.7 times stronger than to GDP-MT, which accounts for the preferential transport of KIF5C into axons and not into dendrites (Nakata et al., 2011). Considering that the MT acts as a nucleotide exchange factor and as a nucleotide activating protein of KIFs, the nucleotide state of the MT might affect both motility and the ATPase kinetics of KIF5C. To examine this possibility, I first analyzed the MT-gliding velocities of monomeric KIF5C motor domain construct K345 [mouse KIF5C residues 1–345 and a 7×His-tag (Okada and Hirokawa, 1999)] using the different nucleotide states of MTs. As shown in Figure 1A, K345 moved along the GMPCPP-MTs at a rate that was 36% faster than that of GDP-taxol-MTs at saturating ATP concentrations [GMPCPP-MT: 338 ± 48 nm/s (mean ± SD) (n = 100); GDP-taxol-MT: 248 ± 44 nm/s (n = 100)]. This difference was statistically significant ($p < 0.001$) and reproducible. The ratio is also conserved in the dimeric KIF5C construct K375 [mouse KIF5C residues 1–375 and a 7×His-tag (Okada and Hirokawa, 1999)] and a previous report (Vale et al., 1994). I then examined the MT-stimulated ATPase activities of K345 to test whether the faster velocity of this kinesin on

GMPCPP-MT is related to a faster rate of ATP hydrolysis. Figure 1B shows that the ATPase activity of K345 stimulated by GMPCPP-MTs was 32% faster than that simulated by GDP-taxol-MTs [kcat (GMPCPP-MT) = 14.3 ± 0.7/s; kcat (GDP-taxol-MT) = 10.8 ± 0.7/s]. This difference in ATPase rates matched the difference in the MT-gliding velocities and explained the faster transport of KIF5C on GMPCPP-MT. In addition, the Michaelis-Menten constants (KM, MT) were not significantly different between the two forms [KM, MT (GMPCPP-MT) = 3.2 ± 0.4 μM; KM, MT (GDP-taxol-MT) = 3.1 ± 0.6 μM], indicating the higher substrate specificity of GMPCPP-MT than GDP-taxol-MT for KIF5C. This suggests that although the conventional kinesin KIF5C could still move well on the GDP-MT stabilized with taxol, GMPCPP-MT is a better substrate for KIF5C.

Cryo-EM Structure of the Nucleotide-Free-KIF5C and GMPCPP-MT Complex

As described above, compared with GDP-taxol-MT, GMPCPP-MT not only binds with high-affinity to KIF5C but also results in faster transport because of the faster ATP hydrolysis cycle, both of which would be crucial for polarized axonal transport in neurons. However, the structural mechanisms explaining how KIF5C distinguishes GTP-MT from GDP-MT and the structural features that correspond to faster ATPase cycling are unknown.

Therefore, I solved the cryo-EM structure of KIF5C complexed with GMPCPP-MT using the previously described real space helical reconstruction (Figure 2A) (Ogura et al., 2014; Yajima et al., 2012). I also solved the KIF5C and GDP-taxol-MT complex, which had already solved by some other groups, to validate the cryo-EM structure solved by this algorithm (Figure 2B) (Atherton et al., 2014; Sindelar and Downing, 2007).

In these structural analyses, KIF5C was forced to release ADP, thereby yielding a nucleotide-free state that is an initial high-affinity binding state to the MT. In the following, I refer to nucleotide-free KIF5C complexed with GMPCPP-MT and GDP-taxol-MT as KIF5(Ø)-CPP-MT and KIF5(Ø)-taxol-MT, respectively.

KIF5C(Ø)-CPP-MT map solved here and KIF5(Ø)-taxol-MT maps solved by Sindelar and Atherton had differences in both KIF5C and MT surface (Figure 2C). On the other hand, no major conformational difference was seen between my KIF5(Ø)-taxol-MT and their KIF5(Ø)-taxol-MT (Figure 2D). Albeit the beta-sheet densities are better separated in the Sindelar's and Atherton's maps, the densities of α-helices of the three KIF5(Ø)-taxol-MT maps were very similar, suggesting that these structures solved by the different algorithms is essentially same each other and that the maps solved by this algorithm are also generally

correct.

The resolutions of KIF5(Ø)-CPP-MT and KIF5(Ø)-taxol-MT were achieved at 8.9 and 9.8 Å, according to the 0.5 criteria of gold-standard FSC using two completely independent map (Figure 3A). The local resolution of KIF5(Ø)-CPP-MT around the neck initial segment (NIS) of neck-linker, nucleotide-binding pocket and the individual loops L5, L7, L9 and L11 were 7-10 Å, and the median resolution of this map was calculated as 8.4 Å (Figure 3B).

Mutual Conformational Adaptation of KIF5C and MT upon their Binding

The overall structure of KIF5(Ø)-CPP-MT was found to closely resemble that of KIF5(Ø)-taxol-MT, albeit with several striking differences in both the KIF5C and MT that were apparent in the statistical analysis. The shapes of the MT-interface of KIF5C were dependent on the nucleotide state of the MT. KIF5C bound to GDP-taxol-MT with the longitudinally long interface as previously reported (Atherton et al., 2014; Sindelar and Downing, 2007), whereas the binding interface for GMPCPP-MT was relatively short and concentrated around the intra-tubulin-dimer groove (bars in Figures 2A and B). The catalytic core of KIF5C was also farther from the surface of GMPCPP-MT than that of GDP-taxol-MT

(Figures 4A and B). On the MT side, several differences were also found among KIF5(Ø)-CPP-MT, KIF5(Ø)-taxol-MT and GMPCPP-MT without KIF5C (CPP-MT), which is previously solved by the same image analysis (Figure 4C) (Yajima et al., 2012). The outer contact, reported to be one of the specific features of GMPCPP-MT, was clearly observed in CPP-MT, whereas it was not observed in KIF5(Ø)-CPP-MT or KIF5(Ø)-taxol-MT. Also the size and shape of the MT holes at which four tubulin monomers meet were different (Figure 4D). In the KIF5(Ø)-taxol-MT or the CPP-MT, the size and shape of the holes alternated between small and large along the protofilament, and is consistent with previous cryo-EM structures. In the KIF5(Ø)-CPP-MT structure, however, the holes were uniform. These findings indicate the distinct longitudinal and lateral contacts among them, suggesting the conformational change in GMPCPP-MT induced by KIF5C binding as well as the effects of the bound nucleotide and taxol to β-tubulins. This overview of the cryo-EM structures collectively illustrated that the binding of KIF5C to GMPCPP-MT induces mutual conformational changes, resulting in strong KIF5C-MT binding that accelerates the release of ADP from KIF5C.

In Silico Docking of the Atomic Models into the Cryo-EM Map

To elucidate the structural mechanism by which KIF5C moves along the MT, the atomic structures of the nucleotide-free KIF5C (PDB ID: 3WRD) (Morikawa et al., 2015) and tubulin-dimer (PDB ID: 1JFF) (Löwe et al., 2001) were docked onto the cryo-EM map of KIF5(Ø)-CPP-MT (Figure 5A). The fitting trials were guided by several parameters, including the cross-correlation coefficient, the average map value, and the number of atoms inside the contour (Figures 5D-G). The volume tracer tool in Sculptor (Birmanns et al., 2011) was also used to detect α-helices from the EM map as references.

For the fitting of KIF5C, the β-sheet core of 3WRD was rigidly fitted into the map, which was followed by the fittings of the switch I helix α3 and switch II helix α4 (Figures 5B, D and E). For the fitting of αβ-tubulins, the reasonable fit for β-tubulin was achieved by rigid body fitting of 1JFF; although, α-tubulin did not fit (dark gray model in Figure 5C). Since most of the differences might be explained by the relative movements among subdomains, the atomic model was divided into three subdomains, the N-domain, I-domain and C-domain, as was the case in a previous report (Yajima et al., 2012), and rigidly docked each one separately (Red and blue models in Figure 5C). To avoid overfitting by introducing extra degree of freedom, several divisions (no division, divided into two, three and four

subdomains) were simulated and the fitting parameters were carefully checked (Figures 5F and G).

The current pseudo-atomic model is still a conservative approximate model. Nonetheless, the positions of most secondary structures are supported by the local maxima of the map density. For further details, see Experimental Procedures.

Conformational Change of MT upon KIF5C Binding

To clarify the conformational change to tubulin, the KIF5(Ø)-CPP-MT was compared with CPP-MT. Remarkable differences were observed especially at the lateral contacts, at the longitudinal contacts, and at the MT surface.

KIF5C was supposed to target the strong intra-dimer interaction that was specifically observed in CPP-MT, between the H4-S5 loop of β-tubulin and H11' and/or H3' of α-tubulin (red broken line in Figure 6A) (Yajima et al, 2012). In the KIF5(Ø)-CPP-MT, KIF5C binds to the rear side of this interaction, the H11' of α-tubulin. As a consequence, the intra-dimer interaction between H4-S5 loop and H11' is broken and instead KIF5C bridges the

intra-dimer groove by connecting the C-domains of α- and β-tubulin (red broken curve in Figure 6B). The direct binding of KIF5C to H11' further pushes the C- and N-domains of α-tubulin downward (Figure 6C), decreasing the surface density at the intra-dimer whereas increasing the density around the nucleotide-binding pocket. This unique compact conformation of α-tubulin that was observed in the KIF5(Ø)-CPP-MT structure for the first time.

The rupture of the strong intra-dimer interaction also triggers a conformational change to the lateral contact between neighboring β-tubulins. In the CPP-MT, helices H3 to H5 (N2-domain) of β-tubulin are raised and separated from H1 and H2 (N1-domain) to form double-layered lateral contacts, the outer contact and the inner contact (Figure 6D). KIF5C-binding then releases the H4-S5 loop of β-tubulin from H11' of α-tubulin so that the N2-domain of β-tubulin becomes flexible (Figure 6E). H3 to H5 of β-tubulin thus rotates downward to fuse these contacts into the single layered canonical lateral contact (Figure 6F).

This rotation further affects the inter-dimer contacts. Helices H11-H11'-H12 (C-domain) of β-tubulin, which locate over the N2-domain, also move downward mainly at their plus-end

half because their minus-end interacts with KIF5C to suppress their movement (Figure 6C). Thus, the surface density had decreased in the KIF5(Ø)-CPP-MT, instead the density around the nucleotide-binding pocket of β-tubulin had increased. As a consequence of these conformational changes, β-tubulin in the KIF5(Ø)-CPP-MT adopts the similar conformation with that in the GDP-taxol-MT, and the I-domain of α-tubulin that interacts β-tubulin to make the inter-dimer contact also resembles to GDP-taxol-MT (Figure 5C).

From these structural analyses, the KIF5C-induced conformational changes to the GMPCPP-MT will affect the strength of the MT-lattice. Thus I tested how KIF5C binding affected the stability of the GMPCPP-MT by examining the shrinking time of GMPCPP-MT with and without KIF5C (Figure 7). As a result, GMPCPP-MT in the presence of KIF5C remained as a filamentous structure much longer than when KIF5C was absent. This suggests that the binding of KIF5C significantly stabilizes the GMPCPP-MT and also supports the conformational change induced by KIF5C binding.

Conformational Change of KIF5C upon KIF5C-MT Binding

As noted above, the conformations of switches I and II changed in the presence and absence

of GMPCPP-MT (Figure 5B). In KIF5(Ø)-CPP-MT, switch I helix α3 adopted a similar conformation to the KIF5 in the ATP form, and switch II was a novel conformation distinct from both the ATP-like and ADP-like forms. Although the loops could not be modeled due to the resolution limit of our map, L5, L7, L8, L9 and NIS may also change their conformation considering from the shape of the map.

The nucleotide-binding pocket in the crystal structure of nucleotide-free KIF5C consists of the shallow groove of the P-loop. In the KIF5(Ø)-CPP-MT cryo-EM map, the P-loop groove is clearly observed at the nucleotide-binding pocket and further deepened by two elements, L5 and L9 (switch I) that approach the pocket to form its top and left walls, respectively (Figure 8A). Interestingly, this switch I conformation (α3-L9) is similar to the crystal structure of KIF5 in the ADP-AlF_4 state complexed with tubulin (Gigant et al., 2013), suggesting that switch I had already acquired the proper conformation to welcome ATP into the pocket (Figure 8B). This conformation is also conserved in the previously solved nucleotide-free KIF5C complexed with GDP-taxol-MT, indicating its functional importance for KIF5C motility (Atherton et al., 2014; Sindelar and Downing, 2007).

On the other hand, switch II helix α4 of KIF5(Ø)-CPP-MT exists distal from the core, both the nucleotide-binding pocket and switch I. This is markedly different from KIF5C of either the ADP-like or ATP-like conformation (Figure 8C). KIF5(Ø)-CPP-MT therefore takes on a third, new type of switch II conformation, which we refer to as the "rigor" conformation in analogy with myosin (Coureux et al., 2003). Since α4 forms the bottom wall of the nucleotide-binding pocket just before the hydrolysis of ATP (Chang et al., 2013), the pocket in the nucleotide-free state lacks the bottom wall for the easy entry of ATP into the pocket. The helix α4 of the rigor conformation becomes shorter from that in the ADP-like conformation, coupled with the elongation of the adjacent L11. The elongated L11, then, squeezes into the space between α4 and α6. The NIS docks to the core to support the raised position of the α4 (Figure 8D). The main driving force for taking the characteristic conformation of α4, therefore, might be the insertion of L11 and the NIS into the space between α4 and α6.

Interface between KIF5C and GMPCPP-MT

Then KIF5-MT interfaces between KIF5(Ø)-CPP-MT and KIF5(Ø)-taxol-MT were compared to examine the different interactions between KIF5C and GMPCPP-MT /

GDP-taxol-MT (Figure 9A). The L8 in all the previously solved KIFs-MT complexes and our KIF5(Ø)-taxol-MT contributes to the interface at the plus-end side of KIF5 that interacts with helix H12 of β-tubulin (Figure 9B). In the KIF5(Ø)-CPP-MT structure, however, the density corresponding to L8 is weak because of the high flexibility of this loop, indicating it is far removed from β-tubulin and is not the main contributor to the KIF5C-GMPCPPMT interaction. This high flexibility of L8 reflects the characteristic short binding-interface of KIF5C on the GMPCPP-MT (Figure 2A).

The most striking difference is the conformation of L11. In KIF5(Ø)-taxol-MT, L11 comes from the left side of α6 and continues toward the plus-end to connect to α4 (Figure 9C). In KIF5(Ø)-CPP-MT, however, L11 passes through the space between α6 and α4, and continues toward the left side to connect to the N-terminus of α4. The thick transverse route of L11 might be stabilized by the interaction with H11' and H12 of α-tubulin, that triggers the mutual adaptation of KIF5C and α-tubulin as described. Loop L12, located on the C-terminal side of α4, also strongly contributes to KIF5C-MT binding (Figure 9D). Our map clearly illustrates its route, which would include its ionic interaction with H12 of β-tubulin.

Another interesting difference at the left, plus-end sides of α4 is the strong connection between KIF5C and β-tubulin, which occurs only for GMPCPP-MT and not for GDP-taxol-MT (Figure 9E). This connection might be made among L7 and α4 of KIF5C, and the loops (H4-S5 and/or H8-S7) at the minus-end side of β-tubulin, with a slight distortion of L7. A similar distortion was reported in the structural neighbor myosin, in which distortion of the β-sheet is necessary for the effective release of ADP (Coureux et al., 2003). Collectively, these observations suggest that the contact between the L7 and β-tubulin, aided by helix α4, will cause a twist of the β-sheet, which in turn will trigger the conformational change of switch I to release ADP from the nucleotide-binding pocket.

L11 is Necessary for Substrate Recognition by KIF5C

The most prominent conformational change at the KIF5C-MT interface involves L11 of KIF5C, which not only serves as a MT interface but also supports the rigor conformation of switch II helix α4. This observation suggested that L11 might be the key player not only in discriminating GTP-MT from GDP-MT but also in determining the fast rate of ATP hydrolysis on GTP-MT. To test this hypothesis, I made the KIF5C swap mutant, KIF5C carrying L11 of KIF1A, and tested the binding affinity for GMPCPP-MT and GDP-MT

(Figures 10A and B). As previously reported, the affinity of the KIF5C catalytic head for GTP-MT was approximately three times higher (Kd = 190 ± 70 nM) than that for GDP-MT (Kd = 500 ± 170 nM) (Nakata et al., 2011; Sweeney and Houdusse, 2010)(Nakata et al, 2011; Sweeney & Houdusse, 2010). However, the L11 swap mutation completely abolished the substrate specificity for GTP-MT vs. GDP-MT, reflected in the similar dissociation constants for GMPCPP- and GDP-MT (Kd = 590 ± 170 nM vs. Kd = 730 ± 210 nM, respectively). These results directly showed that the KIF5C motor head uses L11 to discriminate MT lattice structures differing in their guanine nucleotide content.

Next, the MT-activated ATPase activity of the L11 swap mutant was examined using GMPCPP- and GDP-taxol-MT, to elucidate the contribution of L11 to rapid ATPase cycling in the presence of GMPCPP-MT (Figure 10C). The swap mutation again abolished the difference between GMPCPP- and GDP-taxol-MT. The substrate specificity of the swap mutant, as indicated by the lower MT-concentration area under the curve, was very similar to that of wild-type KIF5C for GDP-taxol-MTs, suggesting that the swapping area of L11 was responsible for the higher substrate specificity of KIF5C for GMPCPP-MT. To further examine whether the charged residues in this swapping area are the main contributor to the

substrate specificity of KIF5C for GMPCPP-MTs, a triple alanine mutation was introduced into the three charged regions in L11 and then measured the activity of its MT-activated ATPase. These triple mutations indeed lessened the difference between GMPCPP- and GDP-taxol-MT, suggesting that at least one of these residues contributes to substrate specificity. However, the alanine mutations also increased the KM, MT for both GMPCPP- and GDP-MT, indicating that one if not all of these residues is involved in the interface common to both GMPCPP- and GDP-taxol-MT. Thus, both the charged and the hydrophobic residues corresponding to those in the area of the swap mutation participate in defining the characteristic function of L11 of KIF5C. In addition, neither the swap mutation nor the alanine mutation affected the basal ATPase activity of KIF5C (Figure 10D), suggesting that the L11 sequence of KIF5C is not involved in this function in the absence of MTs, but it is involved in the MT-activated pathway of the KIF5C ATPase.

Discussion

In this study, I solved the cryo-EM structures of nucleotide-free KIF5C complexed with GMPCPP-MT and GDP-taxol-MT. These structures showed the first detailed structural evidence of mutual conformational changes to KIF5C and GMPCPP-MT upon their interaction.

Implications for Conformational Change of Tubulin Induced by KIF5C Binding.

There have been numerous cryo-EM studies of MT with the various MT-associated proteins including KIFs, albeit no or negligible conformational changes to MTs were reported. The possible reasons for this might be the use of stabilizing reagents for MT, the effect of the bound nucleotide, or the technical limitation to solve the structure. In this study, the GMPCPP-bound MT without any other MT-stabilizing reagent was solved using the single particle based program (Ogura et al., 2014). Although clear evidence is shown here to support a different conformation of MT with and without KIF5C, determining the nature of that new conformation requires higher resolution.

KIF5C binding on GMPCPP-MT generates the downward rotation of N- and C-domains of αβ-tubulin (Figures 6, 11A and 12). These movements lead αβ-tubulin to adopt compact conformations. Interestingly, the I-domains of α- and β-tubulin in the KIF5(Ø)-CPP-MT take very similar conformation with those in the GDP-taxol-MT despite the difference of the nucleotide states as well as the presence/absence of the MT-stabilizing agent taxol (Figure 11B). Considering that I-domain connects the top to the bottom of αβ-tubulin to stabilize or destabilize the longitudinal contact of MT, this I-domain conformation should be one of the energetically stable forms in the straight MT that could be induced by the binding of MT-stabilizing agent to the inside of the MT or the binding of some of the MT-associated proteins to the surface. On the other hand, conformations of N- and C-domains might be altered depending on the bound proteins and reagents, reflecting the distinct surface conformations. In the recently solved KIF5-GMPCPP-MT complex, the tubulin-dimer adopts a similar conformation with that observed in the GDP-taxol-MT (Alushin et al., 2014). Thus, the difference from our structure is the N- and C-domain conformations of α-tubulin. Possible explanations for this difference include the different nucleotide state of KIF5 (nucleotide-free versus a possible ATP-bound state) and the different symmetry of the microtubules (15 PFs four-start versus 13 PFs three-start MTs), albeit the latter is not likely

because the lateral contacts did not differ between them.

A Novel Conformation of KIF5C Bound with GTP-Microtubule

The structural features of nucleotide-free KIF5C in the presence of GMPCPP-MT can be summarized as follows. (1) Switch I (α3-L9) is in the closed conformation. (2) Switch II helix α4 assumes the rigor conformation, in which switch II is distal from the nucleotide-binding pocket. (3) The L11 and NIS are inserted between α4 and α6.

The C-terminus of the helix α3 rotates toward the nucleotide-binding pocket and the elongated L9 covers the pocket (Figures 8A and B). This closed switch I conformation is similar to that of KIF5 holding Mg-ATP in the nucleotide-binding pocket. This means that KIF5C switch I is ready for ATP binding and hydrolysis in the nucleotide-free condition. The rigor conformation of switch II contains the clockwise rotation of α4 around the MT axis, with the elongation of L11 caused by melting of 2.5 turns of the N-terminus of α4 (Figure 8C). Elongated L11 and NIS support the rotation of α4 by squeezing into the space between α4 and α6. NIS is stabilized and points downward, albeit more than two-thirds of the neck-linker remains flexible (Figure 8D). The catalytic core floats above α4 with the help of

L11 and NIS. Switch II helices are thus separate from the nucleotide-binding pocket and from switch I, thereby ensuring that the entrance of the nucleotide-binding pocket is open for ATP entry.

On the GTP-MT, KIF5C tends to adopt the rigor conformation, which enables the effective ATP cycling with the recognition of the specific surface structures of GTP-MT, H4-S5 loop of β-tubulin and H11' of α-tubulin, by the L11 of KIF5C. This specific binding accomplishes a higher specificity of KIF5C to the GTP-MT than to the GDP-MT, and explains a preferential binding to the GTP-MT in the polarized transport of KIF5C to the axon over the dendrites (Nakata et al., 2011).

Conserved Structural Mechanism for ADP Release from KIFs

Among the three features above, only the closed switch I conformation is common between the nucleotide free kinesin-1 on GMPCPP-MT, GDP-taxol-MT, or GDP-tubulin (Atherton et al., 2014; Cao et al., 2014; Shang et al., 2014). Since kinesin-1 moves well both on the GMPCPP-MT and GDP-taxol-MT, albeit with different motility speeds, common structural features between kinesin-1 on two distinct types of MTs may reveal important aspects that

describe the fundamental functionality of kinesin-1 motility. Considering that the α4/L11 serves as the common interface for both types of MTs, there are two possibilities about how the information of MT-binding is conducted from MT to switch I. The first possibility is that the closed switch I might be triggered by MT-binding through the common interface α4/L11. A matter of concern for this is that no contact between switch I and α4/L11 (and even switch II) was observed in KIF5C on the GMPCPP-MT, thus how information of MT-binding is transmitted to switch I is currently unaccountable. The second possibility is that the closed switch I might be triggered through the L7 involved pathway. Kinesin-tubulin contact through L7 was observed in several KIFs, including kinesin-1, kinesin-3 and kinesin-14 (Gigant et al., 2013; Hirose et al., 2006; Nitta et al., 2008). Further structural studies are required to solve the question.

Conformational Variations of KIFs Regulated by the MT

In the previous structural studies and in this work, three conformational variations of each switch I, switch II, and neck-linker were determined (Figure 12). Switch I can assume three conformations, trapped, open and closed. The trapped conformation always includes ADP in the nucleotide-binding pocket, which is surrounded by the Mg-water cap (Nitta et al., 2008).

The open conformation has weakly bound ADP or nothing in the pocket. In the closed conformation, Mg-ATP is in the pocket or the pocket is empty only in the presence of MT. Switch II can also assume three conformations, ADP-like, rigor and ATP-like, that are completely coupled with three conformations of neck-linker, undocked, NIS-docked and docked, respectively. Currently, seven variations of switch I = switch II = neck-linker combinations have been reported: (1) trapped = ADP-like = undocked, (2) open = ADP-like = undocked, (3) open = rigor = NIS-docked, (4) open = ATP-like = docked, (5) closed = ADP-like = undocked, (6) closed = rigor = NIS-docked and (7) closed = ATP-like = docked.

Here, nucleotide-free KIF5 on the GDP-taxol-MT or GDP-tubulin adopts the closed = ADP-like = undocked conformation, whereas nucleotide-free KIF5 on the GTP-MT takes the closed = rigor = NIS-docked conformation (Atherton et al., 2014; Cao et al., 2014; Shang et al., 2014). Since the switch I is responsible for the chemical cycle of kinesins, its conformation might be conserved even on the different type of MTs. Switch II, however, is one of the major interface for the microtubule so that switch II as well as the neck-linker conformations would be altered depending on the difference of the MT conformation. Interestingly, GDP-taxol-MT induces the nucleotide-free Kar3 to take the closed = rigor

conformation, suggesting that the favorable conformation of MT varies with the type of kinesin motors (Hirose et al., 2006). The difference in preference between KIF5 and Kar3 would reflect the biochemical results, which showed that KIF5 tends to stabilize GTP-MT (Figure 6), whereas Kar3 tends to destabilize GDP-MT (Endow et al., 1994).

Finally, we assume the structural model of KIF5C during ADP release cooperates with re-binding (or initial binding) to the GTP-MT and ATP binding cooperates with the power stroke in dimeric motility (Rice et al., 1999) (Figures 11C and 12). In the Mg-ADP state, KIF5C acquires the trapped = ADP-like = undocked conformation, which represents its weak-binding or detached state on/above the MT (Figure 11C (i)). MT-sensing through L7 and/or a4/L11 triggers the transient opening of the nucleotide-binding pocket to release Mg^{2+} and ADP (switch I: open) (Figure 11C (ii)), before taking the closed conformation (Nitta et al., 2008) (Figure 11C (iii)). This switch I movement cooperates with the conformational change of switch II from the ADP-like to the rigor conformation and thus a transition from weak to strong MT binding. With ATP entry and binding, conformational change from the rigor to the ATP-like occurs and produces the power stroke that carries the partner head forward (Figure 11C (iv)). Since the KIF5C structure in the AMPPNP state on the

GMPCPP-MT is still missing, further structural studies are required to clarify this structural model.

Experimental Procedures

Preparation of MT and KIF5C for Cryo-EM

Tubulin was purified from porcine brains by six cycles of polymerization and depolymerization. A high-molarity PIPES buffer was used to remove contaminating MT-associated proteins (Castoldi and Popov, 2003). For GDP-taxol MTs, 18 μM tubulin was incubated in a polymerization buffer (100 mM PIPES, pH 6.8 adjusted with KOH, 1 mM EGTA, 1 mM $MgCl_2$, 1 mM GTP and 6–9% DMSO) at 4 °C for 15 minutes and then clarified by centrifugation at 4 °C for 30 minutes at 100,000 g using a TLA-100.3 rotor (Beckman Coulter) in a TLX ultracentrifuge (Beckman Coulter). The supernatant was polymerized at 37 °C for 60 minutes. Taxol was added in a stepwise fashion to a final concentration of 20 μM. The MTs were collected by centrifugation through a 20% (v/v) glycerol cushion at 37 °C for 15 minutes at 20,000 g and resuspended in PEM-DMSO buffer (100 mM PIPES, pH 6.8 adjusted with KOH, 1 mM EGTA, 1 mM $MgCl_2$ and 6–9% DMSO) containing 20 μM taxol. GMPCPP-MTs were prepared as described previously (Yajima et al., 2012). The KIF5C motor domain construct K345 [mouse KIF5C residues 1–345 and a 7×His-tag; the same construct as K351, used in the previous report (Okada and Hirokawa,

1999)] was expressed in Escherichia coli BL21 (DE3) cells (Novagen) and purified from the cell pellet by immobilized metal affinity chromatography. The eluted fractions were purified further by cation exchange chromatography (AKTA Explorer 10S, RESOURCE S column; GE Healthcare). The purified protein was concentrated in an IMEKOAc buffer (50 mM Imidazole, 5 mM Mg-acetate, 1 mM EGTA, 50 mM K-acetate, pH 7.2 adjusted with HCl), frozen in liquid N_2, and stored at −80 °C.

Cryo-EM

A 5-μl drop of the polymerized MT was placed onto a glow-discharged EM grid (Maxtaform HF35; Pyser-SGI) coated with a perforated carbon film. After 30 seconds, the solution was wicked away with a piece of Whatman no. 1 filter paper and a 5-μl drop of the KIF5C-containing solution (1μM) was quickly applied. After another 30 seconds, this solution was replaced with 2 U apyrase/ml and the mixture was allowed to stand for 60 seconds to obtain a nucleotide-free state. The sample was then washed with IMEKOAc buffer containing 0.1% Triton X-100. Immediately after absorbing the drop by the filter paper, the grid was frozen by plunging it into liquid ethane. The specimens were observed using 200-kV field emission cryo-EM (JEM-2010F; JEOL) with a 626 cryotransfer holder (Gatan,

Inc.). Images were recorded at 40,000-fold magnification on SO163 film (Eastman Kodak Co.), with a defocus of 1200–2600 nm, and developed with D19 (Eastman Kodak Co.) for 10 minutes at 20 °C.

Image Processing and Statistical Analysis

The 15-protofilament and 2-start helix MTs (15-protofilament and 4-start for tubulin monomers) were chosen by their moiré pattern. Selected films were digitized with a charge-coupled device film scanner (Scitex Leafscan45; Leaf Systems) to obtain a final pixel size in the digitized images of 2.5 Å. Image analysis was carried out as previously described (Ogura and Sato, 2006; Ogura et al., 2014; Yajima et al., 2012), with a slight modification in that the high-pass-filtered image was cropped into square pieces of 64 × 64 nm instead of 60 × 60 nm to ensure that the size was sufficient to visualize the kinesin-MT complex. For KIF5(Ø)-CPP-MT and KIF5(Ø)-taxol-MT, >302,000 and >271,000 tubulin dimers were averaged in total, respectively, to achieve the claimed resolution. For estimating resolution, data sets were split in half to make two independent reconstructions and the FSC function was calculated for the whole map (32.5 × 32.5 × 32.5 nm). The statistical significance of differences between KIF5(Ø)-CPP-MT and KIF5(Ø)-taxol-MT maps was examined by

student's t test as described previously (Yajima et al, 2012).

Atomic Model Fitting

The atomic models were fitted in silico to clarify the regions where the major conformational changes occur upon the KIF5C-MT binding. As detailed below, I only performed the rigid body fitting of sub-domains of KIF5C or tubulin due to the resolution limit except for the fitting of the helix α4 of KIF5C whose density was well-separated as a tubular density and also was detected as a helix by the volume tracer tool in Sculptor (Birmanns et al., 2011).

The electron crystallography structure of tubulin [PDB ID: 1JFF, (Löwe et al, 2001)] was used as the initial model for tubulin fitting of our KIF5-GMPCPP-MT map. 1JFF (dimer) was fitted rigidly into the map using Fit in Map tool in UCSF Chimera (Pettersen et al., 2004). However, the dimer model did not fit into the map, thus I separated the 1JFF model into monomers and fitted these two monomers as rigid bodies. As a result, the fitting scores of the average map value (AMV) increased from 160.0 to 161.1, the number of atoms inside the contour increased from 3499 to 3509, and the cross-correlation coefficient (ccc) did not change with a value of 0.699 (Figure 5G). To achieve better fitting, I divided tubulin into four domains pieces, the N1 domain (aa 1–102), N2 domain (aa 103–203), I domain (aa 204–382)

and C domain (aa 383–C terminal). Based on this division, several subdomain fittings were examined; two subdomain fittings (N/IC, N/IC and NI/C), three subdomain fitting (N/I/C), and four subdomain fitting (N1/N2/I/C). Those subdomains were rigidly docked separately and reconnected using MODELLER to satisfy the spatial restraints (Sali and Blundell, 1993). The fitting scores improved to reach a plateau at the three subdomain fitting of α-tubulin (Figure 5F, red). Consequently, I decided to take this docking as a pseudo-atomic model of MT (AMV = 163.5, atoms inside the contour = 3776, ccc = 0.722). Fitting of α-tubulin via the monomer model through to the three subdomain model gave AMV, atoms inside the contour and ccc varied from 160.7 to 164.8, from 1697 to 1920 and from 0.706 to 0.746, respectively. On the other hand, subdividing β-tubulin gave the little additional improvement of fittings with the little alteration of the fitting parameters; those scores of β-tubulin (monomer fitting through to four subdomain fitting) increased from 160.9 to 162.7 (AMV), from 1802 to 1856 (atoms inside the contour), and from 0.708 to 0.718 (ccc) (Figure 5F, blue). The helices H11 and H12 in the newly created atomic model of α-tubulin matched the helical densities detected by the volume tracer tool in Sculptor, also supporting the validity of this fitting.

For the density of KIF5C, the X-ray crystal structure of nucleotide-free KIF5C (PDB ID:

3WRD) (Morikawa et al., 2015) was used as the initial model (AMV = 154.0, atoms inside the contour = 882, ccc = 0.713) (Figure 5E). Since the map corresponding to the switch I region (aa 177–205), in which the nucleotide-free KIF5C crystal model did not fit, was preferably similar to the map of KIF5(ADP-Mg-AlFx)-MT, I rigidly fit the switch I region by referring to the 4HNA structure. This fitting of switch I (PDB ID: 4HNA) enabled us to obtain better fitting scores of α3. The AMV increased from 146.6 to 152.6, atoms inside the contour from 39 to 40, and the ccc from 0.322 to 0.330 (Figure 5D, green). To fit switch II (aa 233–296), especially helix α4, which was different between the crystal structure and the cryo-EM structure, the volume tracer tool in Sculptor was used to find a possible helical density corresponding to α4. I then moved and fit the switch II α4 to the detected helical density using the Fit in Map tool. Through these fittings, the AMV of the α4 increased from 147.6 to 158.7, atoms inside the contour increased from 24 to 34 and the ccc from 0.274 to 0.302 (Figure 5D, chartreuse). Fragmented models were reconnected, and finally, the KIF5 atomic model was found to fit well to the map (AMV = 156.8, atoms inside contour = 948, ccc = 0.740) (Figure 5E). I finally confirmed that the model had no steric clashes by the ADIT deposition tool. As a consequence, I got a pseudo-atomic model of KIF5(Ø)-CPP-MT, which fits in the map in the similar level as previously published models.

Preparation of Kinesin L11 Mutants

Mutated K345 with a C-terminal reactive cysteine tag (-RKRCR-) was generated by overlapping PCR using the K345 expression vector as the template. The final PCR product was checked by DNA sequencing before it was cloned into the pET21b expression vector (Novagen). The protein was expressed in E. coli BL21 (DE3) cells and purified by immobilized metal affinity chromatography. For the binding assay, wild-type K345 and its mutants were labeled with Alexa 594 maleimide (Invitrogen).

Binding Assay

Purified tubulin was labeled with Alexa Fluor 488 or 647 succinimidyl ester (Invitrogen) as described previously (Desai and Mitchison, 1998). Labeled tubulin was mixed with unlabeled tubulin such that 10% of the tubulin was labeled with the Alexa Fluor dye. After 15 min incubation on ice, the mixture was clarified and polymerized to yield GMPCPP-MT and GDP-MT. Labeled GMPCPP-MT and GDP-MT were then mixed at a ratio of 1:1 in assay buffer (80 mM PIPES, pH 6.8, adjusted with KOH, 0.8 mM EGTA, 0.8 mM $MgCl_2$, 20% glycerol, 2 mM AMPPNP, 1 mM glucose, 0.2 mg glucose oxidase/ml, 0.04 mg catalase/ml

and 5 mM cysteamine). The Alexa Fluor 594-labeled kinesin or the mutants was then mixed into the MT solution to varying final concentrations (15–1500 nM). For the nucleotide-free state, 2 U apyrase/ml was added to the buffer. After incubation at 37 °C, the kinesin-MT mixture was spread onto the cover glass and glutaraldehyde was added to a final concentration of 2.5% to stop MT depolymerization. The specimen was observed using the ELYRA P.1 system (Carl Zeiss, Jena, Germany) in the TIRF mode.

Gliding Assay

MT gliding assays were performed as described previously (Carter and Cross, 2001), with a slight modification. In brief, a flow chamber assembled from a glass slide and a coverslip was coated with a penta-His antibody (Qiagen) for 3 min and washed with PEM buffer (100 mM PIPES, pH 6.8 adjusted with KOH, 1 mM EGTA and 1 mM $MgCl_2$). Then, 0.1 mg of kinesin/ml was introduced to allow its immobilization at the C-terminal His-tag. The chamber was then washed and blocked with casein-containing PEM buffer (1 mM DTT, 20 μM taxol for GDP-taxol-MT and 2 mg casein/ml in PEM buffer). Subsequently, the MT solution was injected into the chamber together with the motility buffer (1 mM DTT, 20 μM taxol for GDP-taxol-MT, 2 mg casein/ml, 5 mM Mg-ATP and 5 mg glucose/ml in PEM buffer) and an

oxygen scavenging system consisting of 0.05 mg glucose oxidase/ml and 0.1 mg catalase/ml. Time-lapse images were acquired using the ELYRA P.1 system in the TIRF mode at 37 °C.

ATPase Assay

ATPase activity was assayed at 25 °C with the EnzChek phosphate assay kit (Molecular Probes) using a spectrophotometer (V630-Bio, JASCO). MT-activated ATPase activity was measured in PEM buffer containing 20 nM K345, varying concentrations of MT (0–20 μM) and 2 mM Mg-ATP. Basal ATPase activity was determined in PEM buffer containing 2 μM K345 and 0–5 mM Mg-ATP.

MT Shrinking Assay

Labeled tubulin was mixed in a 1:5 molar ratio to unlabeled tubulin and incubated in polymerization buffer (100 mM PIPES, pH 6.8 adjusted with NaOH, 1 mM EGTA, 1 mM $MgCl_2$, 6% DMSO and 1 mM GMPCPP) at 37 °C for 2 h. Labeled GMPCPP-MT and K345 were mixed with 5 mM AMPPNP and the mixture was spread onto a coverslip. Time-lapse observations were performed at room temperature using TIRF as described in the sections above and measured the duration until depolymerization began. GMPCPP-MTs polymerized

with PIPES adjusted with KOH were also tested and showed similar tendencies as was observed for NaOH (Figure 7), albeit spending much longer periods.

Accession numbers

The cryo-EM map and the coordinate solved in this study have been deposited in the Electron Microscopy Data Bank and Protein Data Bank as EMD-5916 and PDB ID 3J6H.

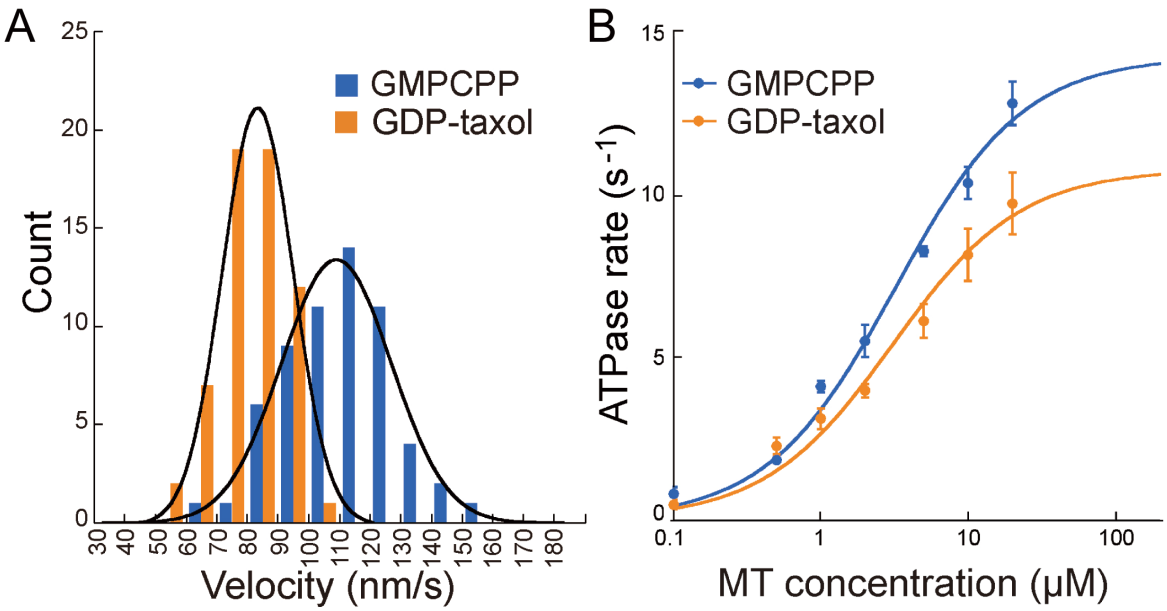

Figure 1. Effects of Nucleotide-state in MT on KIF5C Motility and Kinetics.

(A, B) Gliding assays (A) and ATPase activity assays (B) of KIF5C on GMPCPP-MT (blue) and GDP-taxol-MT (orange). Error bars in (B) are the SEM of at least four independent measurements.

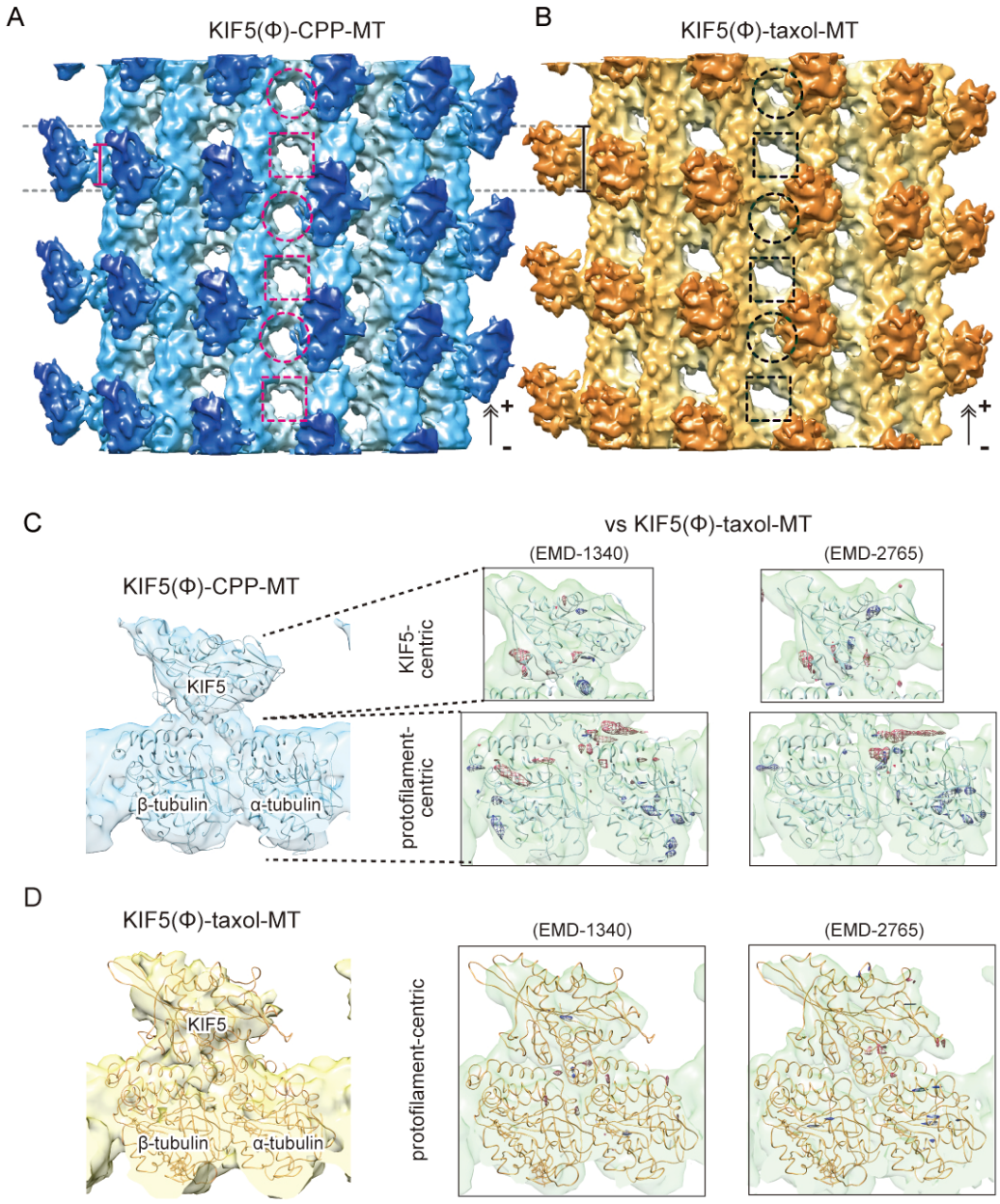

Figure 2. Cryo-EM Structure of the KIF5C-MT Complex.

(A, B) Cryo-EM structures of KIF5(Ø)-CPP-MT (A) and KIF5(Ø)-taxol-MT (B). The bars represent the length of the KIF5-MT interface. The dashed circles and squares indicate the holes surrounded by intra-tubulin-dimers and inter-tubulin-dimers, respectively.

(C, D) KIF5C(Ø)-CPP-MT (C) and KIF5C(Ø)-taxol-MT (D) solved in this study were compared to KIF5B(Ø)-taxol-MT solved previously (EMDB: 1340 and 2765) (Atherton et al., 2014; Sindelar and Downing, 2007) with the difference map ($\sigma \approx 2.0$, red and blue). The red/blue mesh maps show the increase/decrease density in the previous maps. KIF5(Ø)-CPP-MT pseudoatomic model and the deposited atomic model (4UXO, orange) (light blue) were docked in maps.

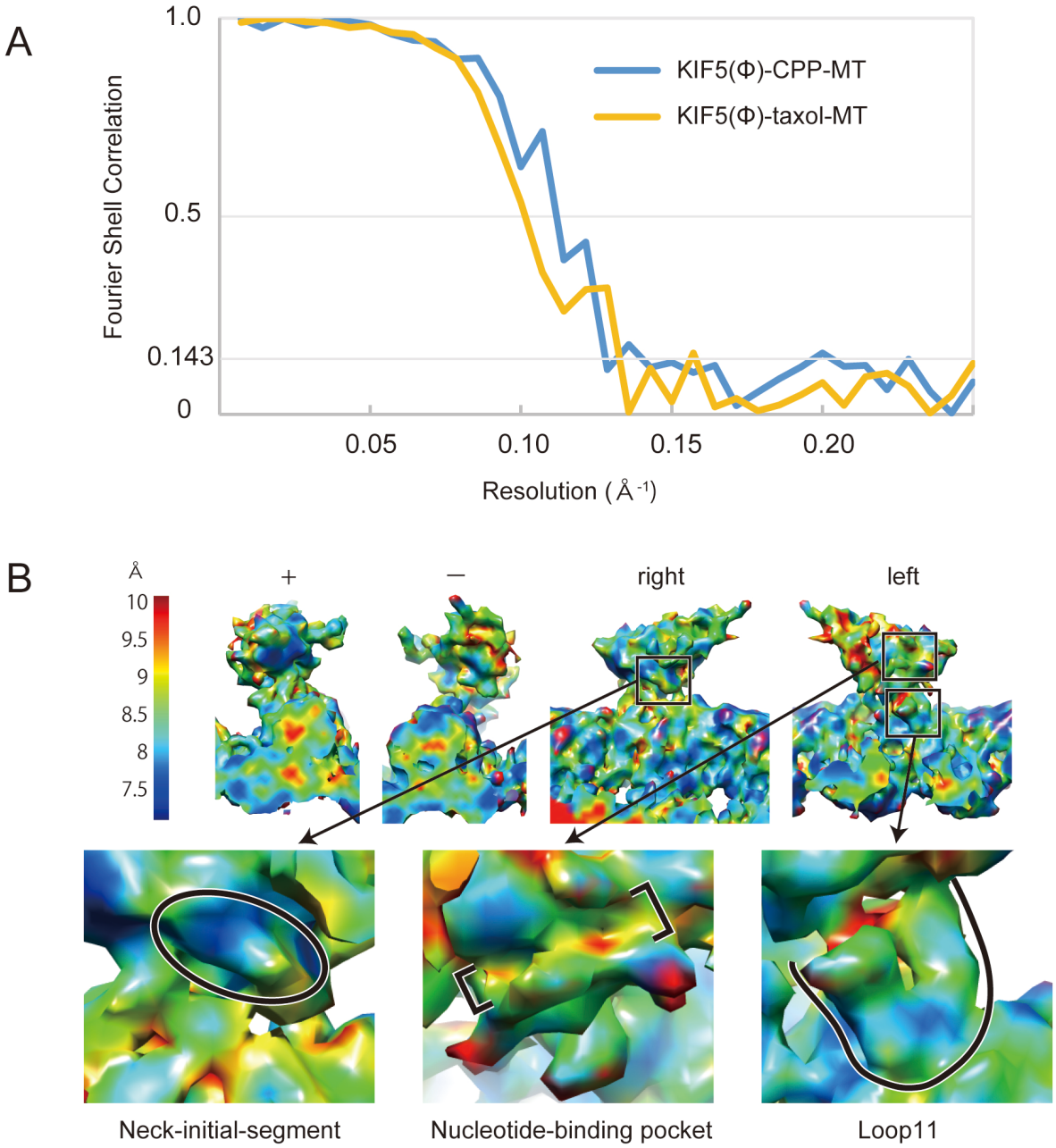

Figure 3. Resolutions of Cryo-EM Maps.

(A) Gold-standard FSC curves.

(B) Local resolution of KIF5(Ø)-CPP-MT calculated by ResMap. The median resolution is 8.4 Å.

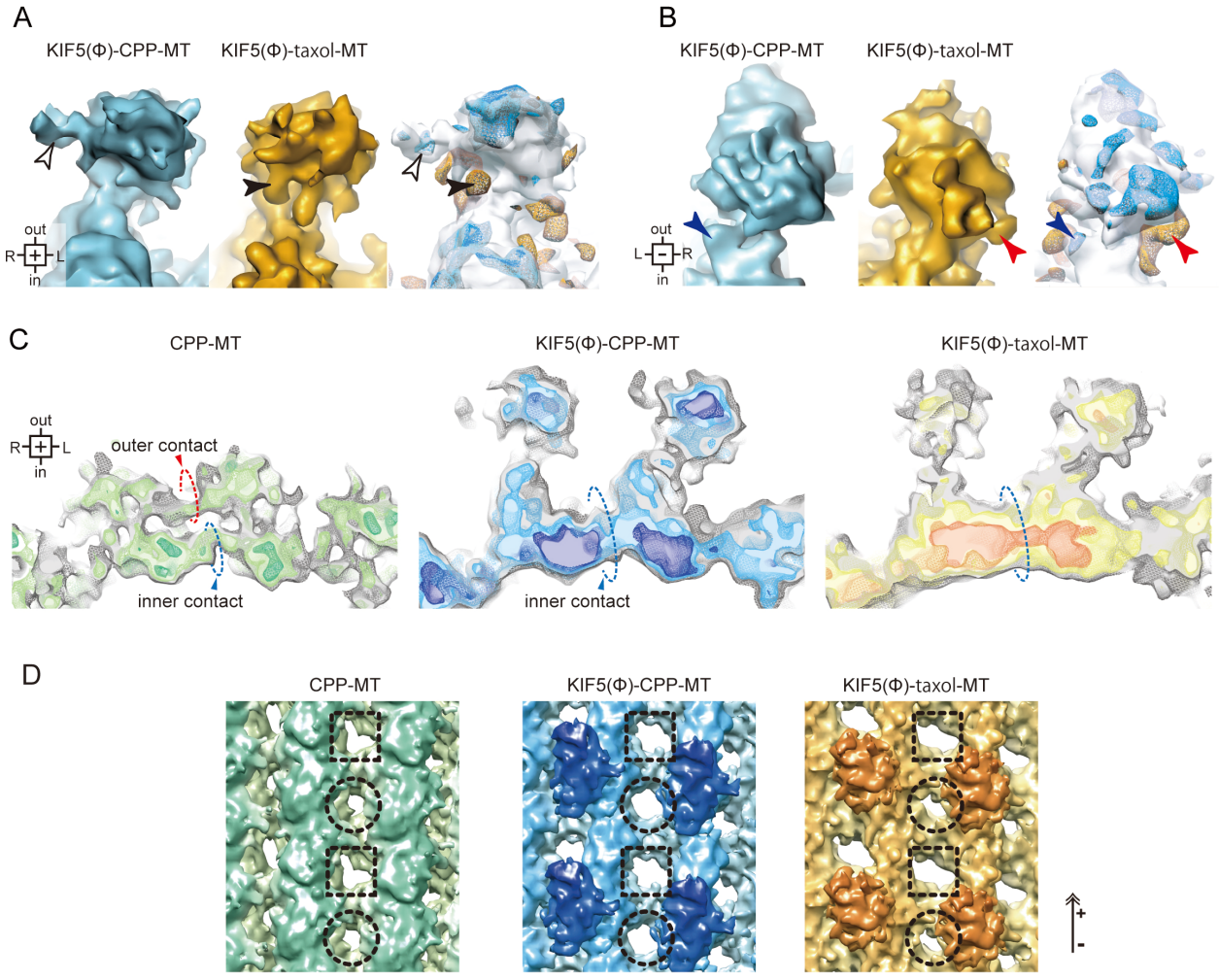

Figure 4. Overall Comparison of Cryo-EM Structures.

(A, B) Magnified views of KIF5C seen from the plus (A) and minus (B) end. KIF5(Ø)-CPP-MT (blue), KIF5(Ø)-taxol-MT (orange), and the statistical significance of their differences (t-map, n=46). The blue and orange meshes of the t-maps show the densities increase in maps of each color. $P < 10^{-2.5}$ was defined as significant. Arrowheads indicate the regions differ significantly.

(C) Cross-sectional views of CPP-MT, KIF5(Ø)-CPP-MT and KIF5(Ø)-taxol-MT, seen from the plus-end. Dashed circles indicate lateral contacts.

(D) Surface conformation of CPP-MT, KIF5(Ø)-CPP-MT and KIF5(Ø)-taxol-MT. Dashed circles show the holes of intra-tubulin-dimer interfaces, and the squares show the holes of inter-tubulin-dimer interfaces. The size and shape of the holes of MTs were affected by kinesin binding, GTP hydrolysis of β-tubulin and taxol binding, suggesting that the conformational changes of tubulin were induced to alter both the longitudinal and the lateral contacts.

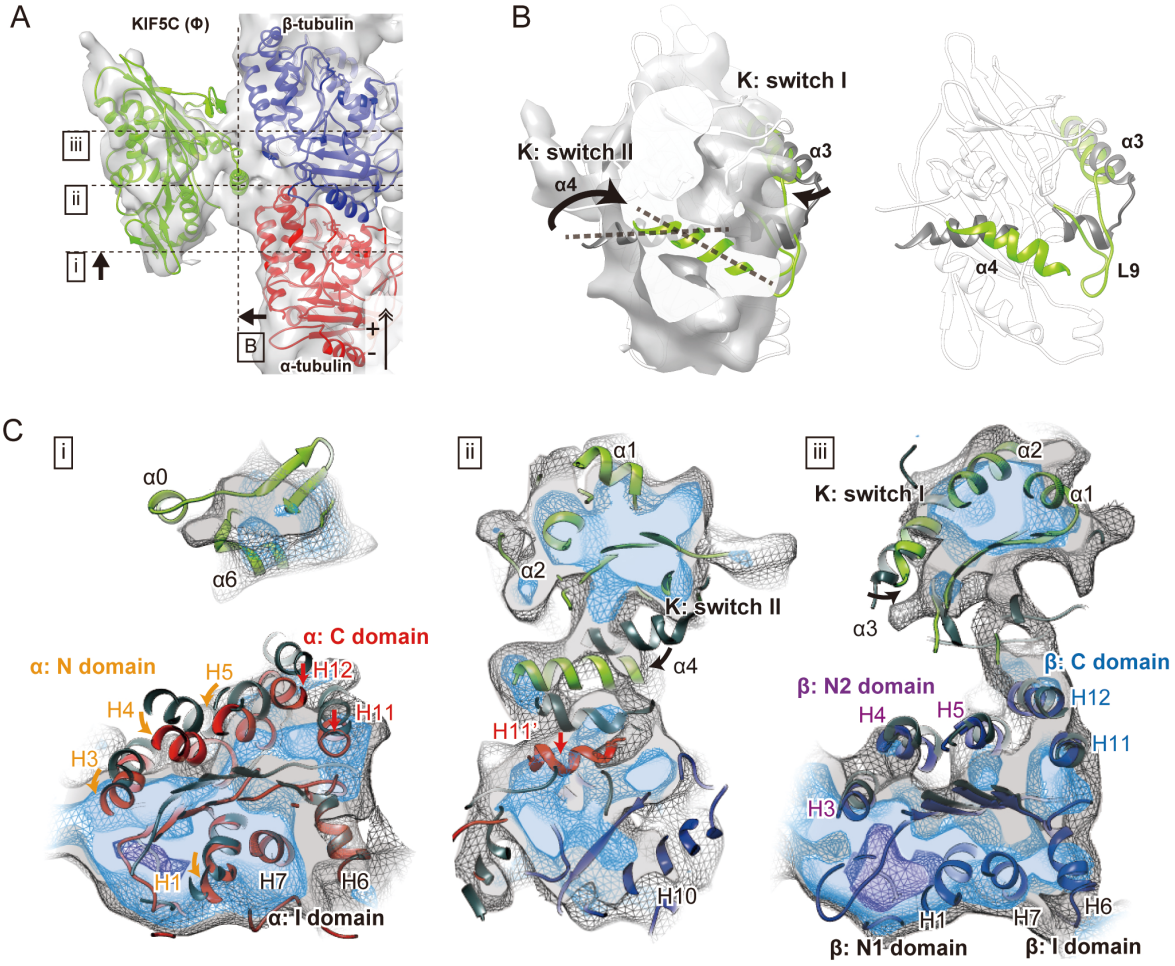
A
KIF5C (Φ)
β-tubulin
iii
ii
i
B
α-tubulin
+
-
B
K: switch I
K: switch II
α3
α4
α4
L9
C
i
α0
α6
α: N domain
α: C domain
H5
H12
H4
H11
H3
H1
H7
H6
α: I domain
ii
α1
α2
K: switch II
α4
H11'
H10
iii
α2
K: switch I
α1
α3
β: C domain
β: N2 domain
H4
H5
H12
H11
H3
H1
H7
H6
β: N1 domain
β: I domain

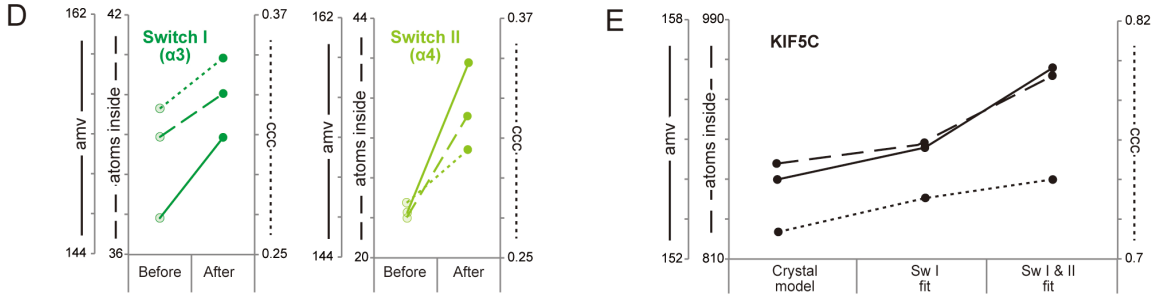
D
Switch I (α3)
Switch II (α4)
amv
atoms inside
ccc
Before
After
E
KIF5C
Crystal model
Sw I fit
Sw I & II fit

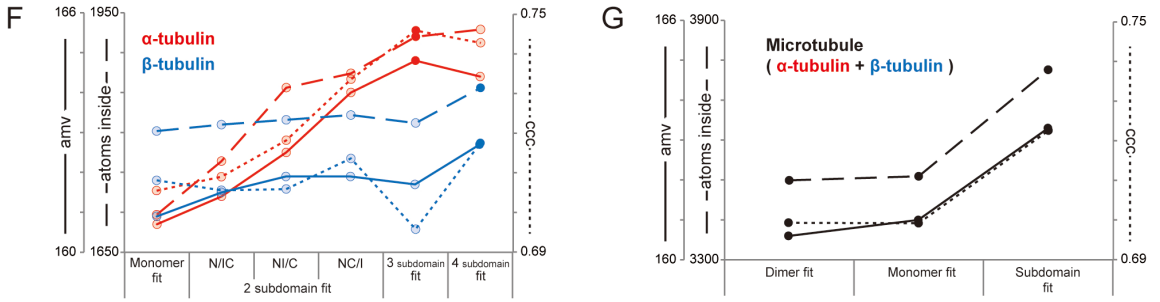
F
α-tubulin
β-tubulin
amv
atoms inside
ccc
Monomer fit
N/IC
NI/C
NC/I
3 subdomain fit
4 subdomain fit
2 subdomain fit
G
Microtubule
(α-tubulin + β-tubulin)
Dimer fit
Monomer fit
Subdomain fit

Figure 5. Atomic Model Docking into KIF5(Ø)-CPP-MT Map.

(A) Pseudo-atomic model fitted into the KIF5(Ø)-CPP-MT for the orientation of (B) and (C).

(B) Cross section seen from the MT-binding side (left) and the comparison of the models (right). The gray model indicates the KIF5(Ø) crystal structures (PDB ID: 3WRD) before the subdomain fittings.

(C) Cross sections seen from the minus-end. Dark gray models indicate the tubulin-dimer (PDB ID: 1JFF) and KIF5(Ø) crystal structure (PDB ID: 3WRD) before the subdomain fittings.

(D) The three parameters, average map value (solid line), atoms inside the contour (dashed line) and cross-correlation coefficient (dotted line) of the α3 and α4 before and after the subdomain fitting of 3WRD.

(E) Fitting curves of KIF5 from the overall-rigid body fitting to the subdomain fittings.

(F) The local fitting scores comparing the 1(monomer), 2 (N/IC, NI/C and NC/I), 3 (N/I/C), and 4 (N1/N2/I/C) subdomain fittings of α-tubulin (red) and β-tubulin (blue). The 3 subdomain fitting and 4 subdomain fitting were chosen as final models for α- and β-tubulin, respectively (dark color plots).

(G) Transition of fitting parameters for one tubulin dimer through the docking trails. "Subdomain fit" means the union of 3 subdomain fitting of α-tubulin and 4 subdomain fitting of β-tubulin.

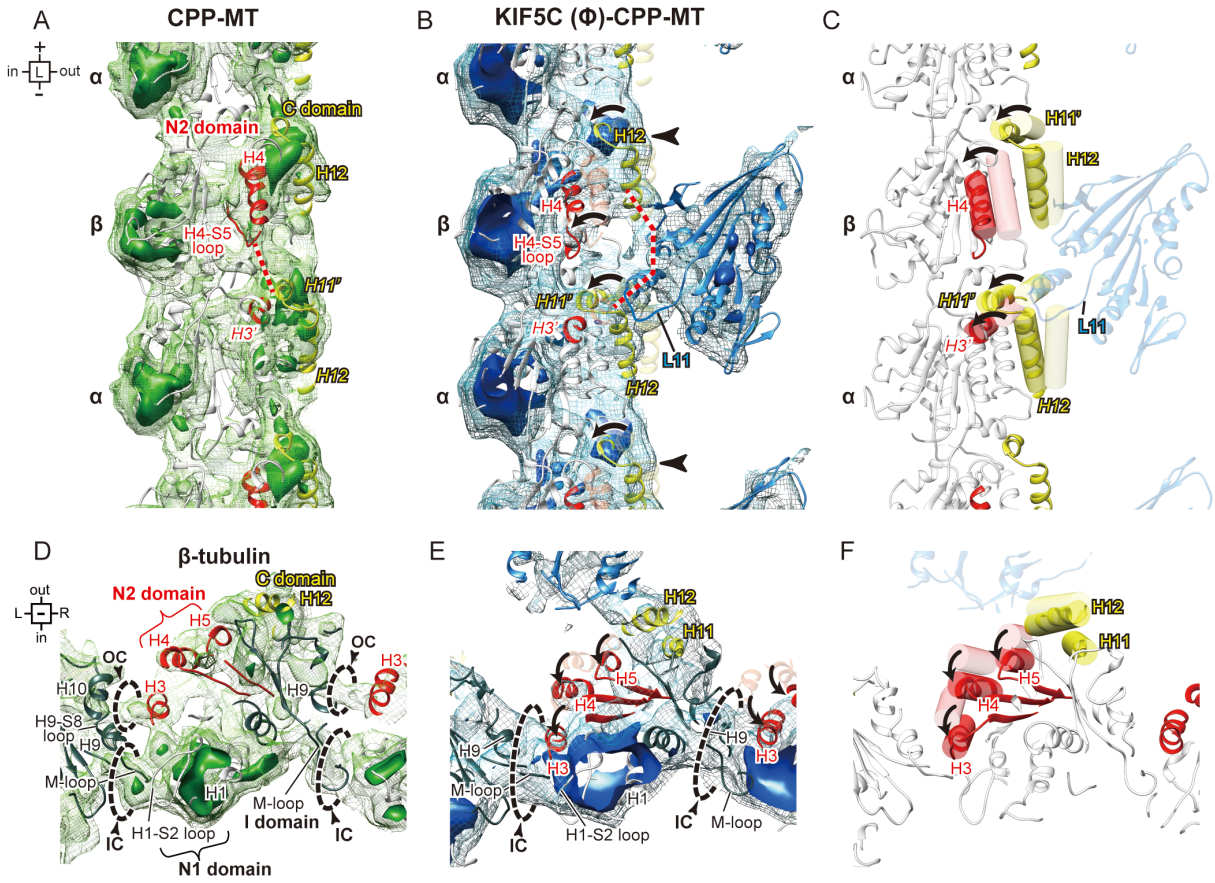

Figure 6. KIF5C-Induced Conformational Change of GMPCPP-MT.

(A, B) The left side view of CPP-MT (A) and KIF5(Ø)-CPP-MT (B), with three different contour levels and at the same resolution (8.9 Å). Mesh, 1.3 σ; light color, 1.5 σ; dark color, 1.8 σ. The arrowheads indicate the major difference on the MT surface at the minus-end of α-tubulin.

(C) KIF5C-induced movements of helices in N2-domain (red) and C-domain (yellow).

(D, E) CPP-MT (D) and KIF5(Ø)-CPP-MT (E), seen from the MT minus-end at the level of β-tubulin. OC, outer contact; IC, inner contact.

(F) KIF5C-induced movements of helices in N2-domain (red) and C-domain (yellow) of β-tubulin.

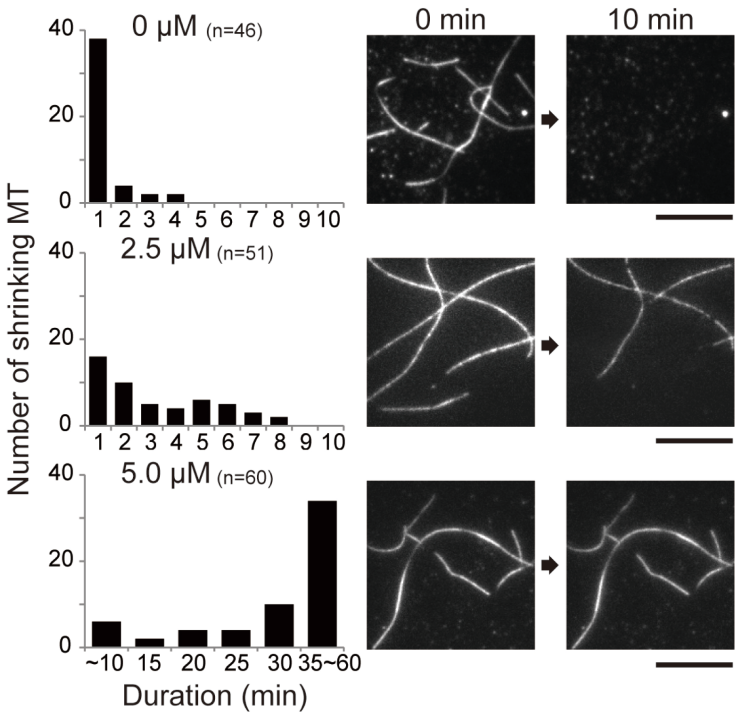

Figure 7. Effect of KIF5C Binding on GMPCPP-MT Stability.

Shrinking rates of GMPCPP-MT with various concentrations (0, 2.5 and 5.0 µM) of KIF5C. The number of MTs which began to shrink in the duration are counted. Right panel depicts representative TIRF images at 0 min (left) and 10 min (right). Bar, 10 µm.

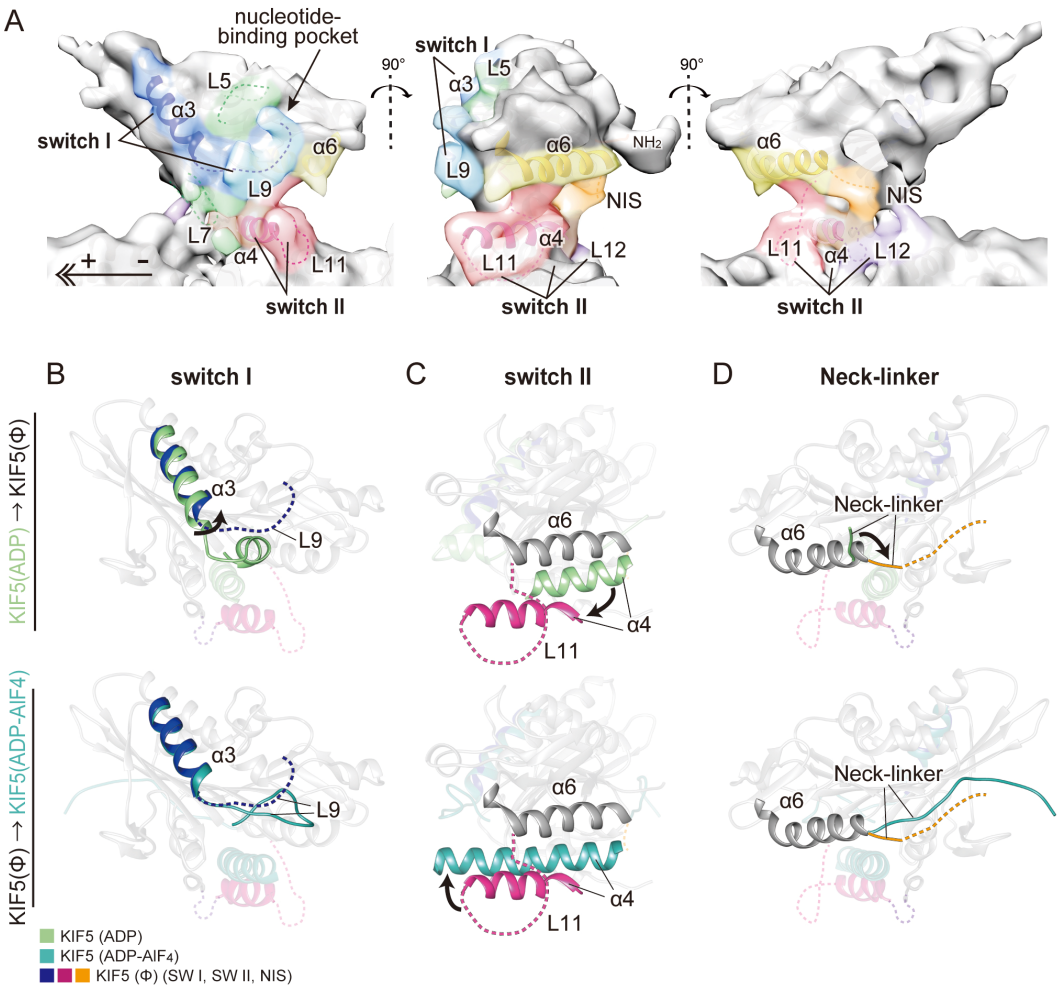

Figure 8. Conformational Changes of KIF5C on GMPCPP-MT.

(A) Cryo-EM map of KIF5(Ø)-CPP-MT, as seen from the left (left), minus-end (middle) and right (right).

(B) Comparison of the switch I conformation to that of KIF5(ADP) (ADP-like conformation, PDB ID: 1BG2) (upper panel) and KIF5(ADP-AlF_4) (ATP-like conformation, PDB ID: 4HNA) (lower panel), as seen from the left. Blue, nucleotide-free KIF5C switch I; light green, 1BG2; dark cyan, 4HNA.

(C) Comparison of the switch II conformations as seen from the MT-minus end. Magenta, nucleotide-free KIF5C switch II; light green, 1BG2; dark cyan, 4HNA.

(D) Comparison of neck-linkers (NIS) as seen from the right. Orange, nucleotide-free KIF5C neck-linker; light green, 1BG2; dark cyan, 4HNA.

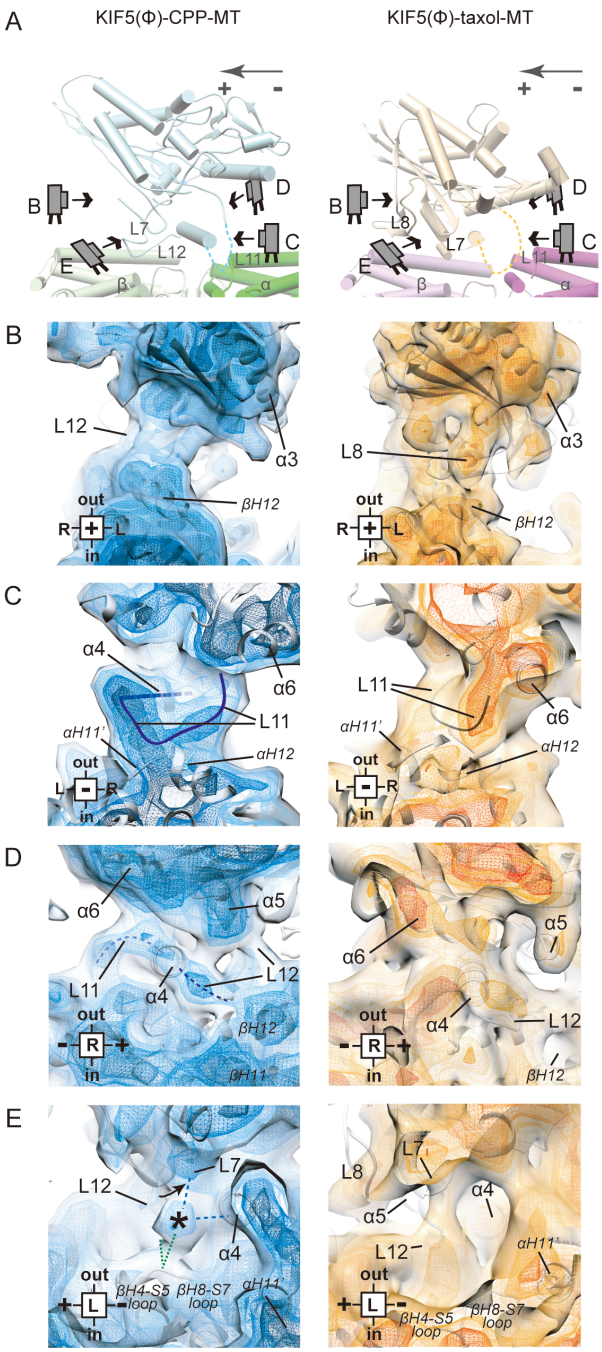

Figure 9. Interface Between KIF5C and MT.

(A) Cartoon representation of KIF5C complexed with GMPCPP-MT (left) and GDP-taxol-MT (rihgt) for orientation in the following panels.

(B-E) The differences of the L8 contribution to the KIF5C–MT interaction (B), the routes and the positions of L11 and α6 (C), the conformations of L12 and α6 (D), and the interaction between L7 and α4 of KIF5C and the loops of β-tubulin (E). Blue map, KIF5(Ø)-CPP-MT; orange map, KIF5(Ø)-taxol-MT. Four different contour levels are shown. Light surface, 1.3 σ; light mesh, 1.35 σ; medium mesh, 1.43 σ; dark mesh, 1.5 σ.

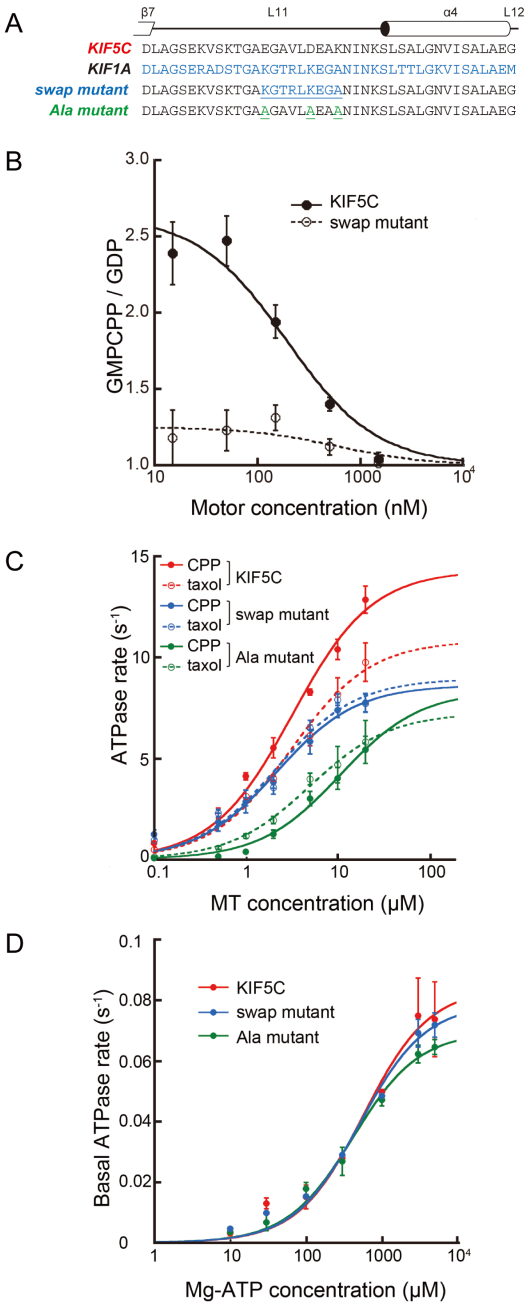

Figure 10. Importance of L11 to Discriminate GTP-MT from GDP-MT.

(A) Sequence alignments of KIF5C, KIF1A and the KIF5C L11 mutants.

(B) Binding assays of KIF5C and swap mutant in the nucleotide-free state. The ratio of MT-bound KIF5C vs. GMPCPP-MT and GDP-MT is plotted against the motor concentration. The mean and SEM were measured from 120 MTs at each point.

(C) ATPase activities of KIF5C (red) and the swap (blue) and Ala (green) mutants with GMPCPP-MT (solid lines) and GDP-taxol-MT (broken lines). Wild-type data are the same as in Figure 1B.

(D) Basal ATPase activities. Error bars are the SEM of at least four independent experiments.

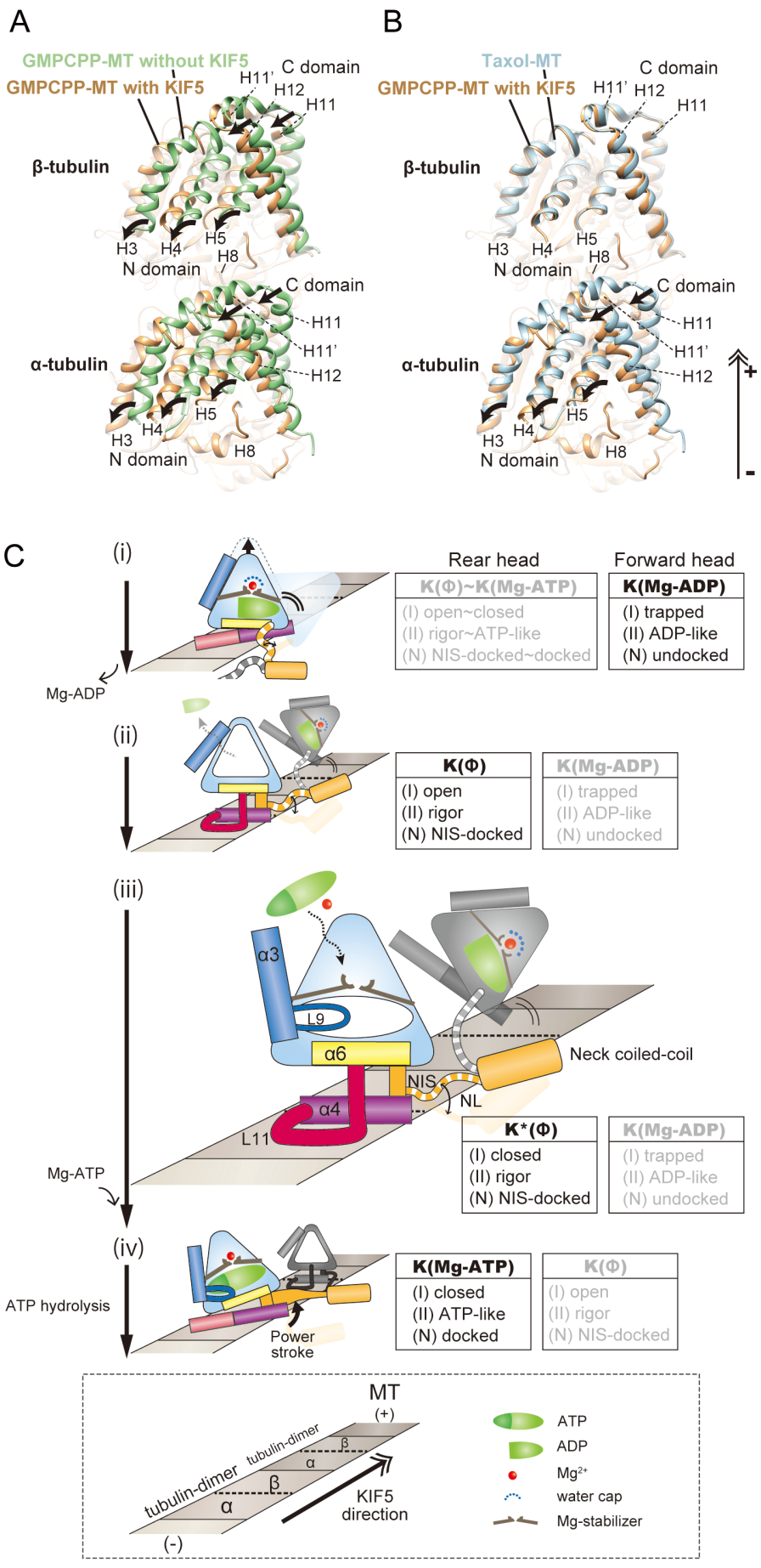
A
GMPCPP-MT without KIF5
GMPCPP-MT with KIF5
C domain
H11'
H12
H11
β-tubulin
H3
H4
H5
H8
N domain
C domain
H11
H11'
H12
α-tubulin
H5
H4
H3
N domain
H8
B
Taxol-MT
GMPCPP-MT with KIF5
C domain
H11'
H12
H11
β-tubulin
H3
H4
H5
H8
N domain
C domain
H11
H11'
H12
α-tubulin
H5
H4
H3
N domain
H8
+
-
C
(i)
Rear head
Forward head
K(Φ)~K(Mg-ATP)
(I) open~closed
(II) rigor~ATP-like
(N) NIS-docked~docked
K(Mg-ADP)
(I) trapped
(II) ADP-like
(N) undocked
Mg-ADP
(ii)
K(Φ)
(I) open
(II) rigor
(N) NIS-docked
K(Mg-ADP)
(I) trapped
(II) ADP-like
(N) undocked
(iii)
α3
L9
α6
NIS
NL
α4
L11
Neck coiled-coil
K*(Φ)
(I) closed
(II) rigor
(N) NIS-docked
K(Mg-ADP)
(I) trapped
(II) ADP-like
(N) undocked
Mg-ATP
(iv)
ATP hydrolysis
Power stroke
K(Mg-ATP)
(I) closed
(II) ATP-like
(N) docked
K(Φ)
(I) open
(II) rigor
(N) NIS-docked
MT
(+)
tubulin-dimer
β
α
tubulin-dimer
β
α
KIF5 direction
(-)
ATP
ADP
Mg2+
water cap
Mg-stabilizer

Figure 11. Schematic Representation of the Conformational Changes in GTP-MT and Kinesin.

(A) Comparison of MT structures between KIF5(Ø)-CPP-MT (brown) and CPP-MT (green). KIF5C induces the downward movement of C/N domains of α- and β-tubulin.

(B) Comparison of MT structures between KIF5(Ø)-CPP-MT and GDP-taxol-MT (PDB ID: 1JFF). KIF5C induces the downward movement of C/N domians of α-tubulin. β-tubulin structures are very similar between them.

(C) Schematic model for the ATPase cycle in the dimeric kinesin motility on GTP-MT. In the Mg-ADP state, switch II acquires the ADP-like conformation with the flexible neck-linker, which represents the weak-binding state on the MT (i). Then nucleotide-binding pocket opens to release Mg^{2+} and ADP (ii). After releasing Mg^{2+} and ADP, switch I adopts closed conformation to hold the next Mg-ATP (iii). Switch II takes the rigor-conformation which is supported by the docked NIS and elongated L11. Switch II is distant from switch I, thus Mg-ATP enter the nucleotide-binding pocket. Mg-ATP binding allows neck-linker docking and produces the power stroke that carries the partner head (gray model) forward (iv).

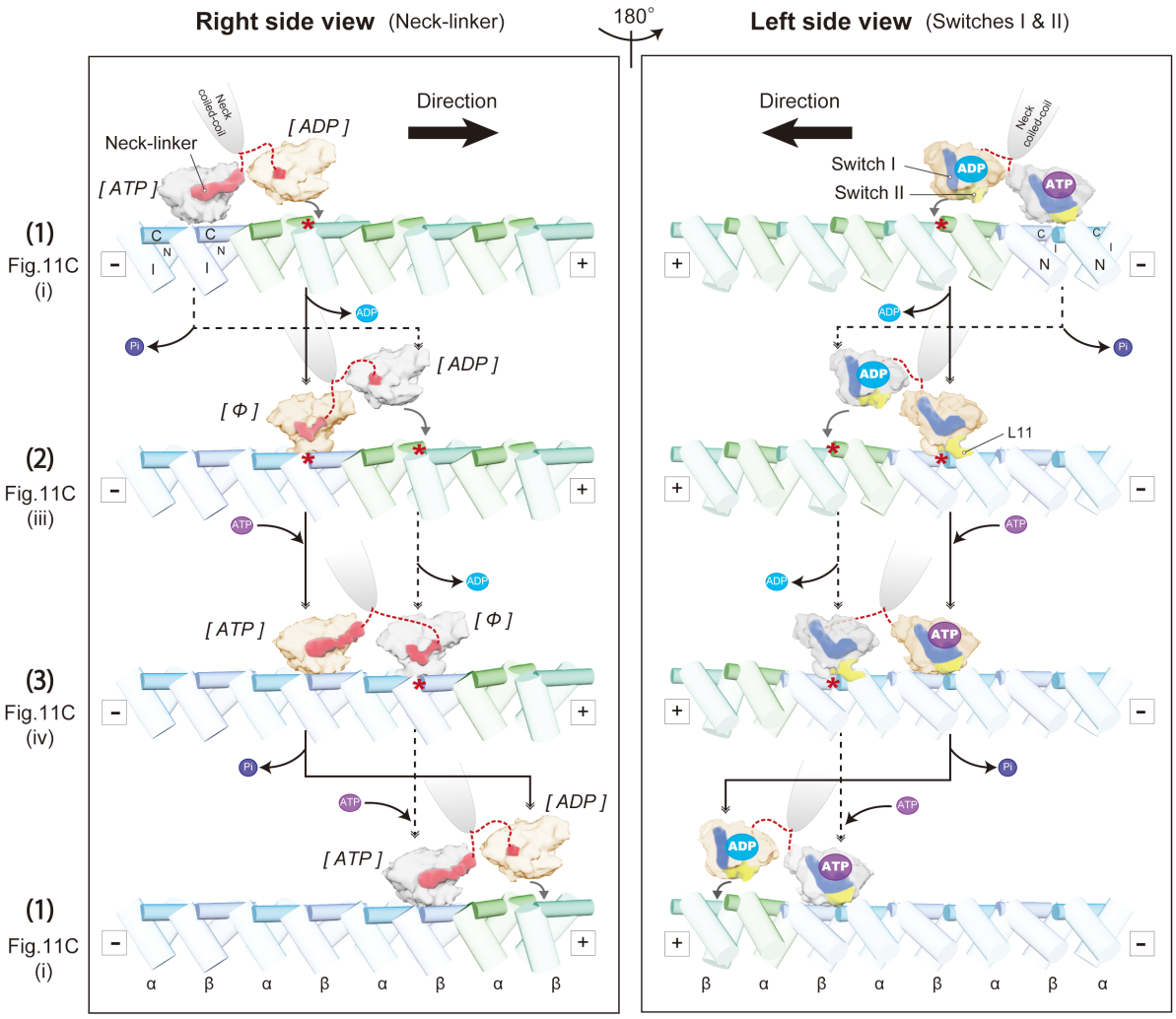

Figure12. Movements of switches I, II, neck-linker and GTP-MT through kinesin stepping.

Dimeric kinesin has two catalytic heads that are connected through a neck-linker (red) and neck coiled-coil stalk. Each catalytic head contains nucleotide-binding domain "switch I" (blue), and MT-binding domain "switch II" (yellow). In order not to dissociate from MT along the stepping, switch I, switch II, and neck-linker change their conformations as a coordinated manner for each nucleotide hydrolysis cycle. The movement of the neck-linker and switches I and II can be observed, respectively, from the right side and left side. From ADP state (orange head in (1)) to ATP state (orange head in (3)), via nucleotide-free state (orange head (2)), the neck-linker gradually dock to the core fixing the other head (the gray head) forward. During this process, the gray head detaches from the MT by hydrolyzing ATP, strokes, and attaches again to the MT by releasing ADP. The conformation solved in this cryo-EM study is the rear head of the step 2, or the forward head of the step 3. The neck-linker at this state is half-docked, switch I is closed, and switch II attaches to the C-domain of the MT through L11 (the rigor conformation). The L11 causes the downward

movement of the C-domain and then N-domain of the GTP-MT (red asterisks), making the GTP-MT lattice strong like taxol-stabilized GDP-MT.

References

Alonso, M. C., D. R. Drummond, S. Kain, J. Hoeng, L. Amos, and R. A. Cross, 2007, An ATP gate controls tubulin binding by the tethered head of kinesin-1: Science, v. 316, p. 120-3.

Alushin, G. M., G. C. Lander, E. H. Kellogg, R. Zhang, D. Baker, and E. Nogales, 2014, High-Resolution Microtubule Structures Reveal the Structural Transitions in $\alpha\beta$-Tubulin upon GTP Hydrolysis: Cell, v. 157, p. 1117-29.

Asbury, C. L., A. N. Fehr, and S. M. Block, 2003, Kinesin moves by an asymmetric hand-over-hand mechanism: Science, v. 302, p. 2130-4.

Atherton, J., I. Farabella, I. M. Yu, S. S. Rosenfeld, A. Houdusse, M. Topf, and C. A. Moores, 2014, Conserved mechanisms of microtubule-stimulated ADP release, ATP binding, and force generation in transport kinesins: Elife, v. 3.

Birmanns, S., M. Rusu, and W. Wriggers, 2011, Using Sculptor and Situs for simultaneous assembly of atomic components into low-resolution shapes: J Struct Biol, v. 173, p. 428-35.

Block, S. M., L. S. Goldstein, and B. J. Schnapp, 1990, Bead movement by single kinesin molecules studied with optical tweezers: Nature, v. 348, p. 348-52.

Cao, L., W. Wang, Q. Jiang, C. Wang, M. Knossow, and B. Gigant, 2014, The structure of apo-kinesin bound to tubulin links the nucleotide cycle to movement: Nat Commun, v. 5, p. 5364.

Carter, N., and R. Cross, 2001, An improved microscope for bead and surface-based motility assays: Methods Mol Biol, v. 164, p. 73-89.

Castoldi, M., and A. V. Popov, 2003, Purification of brain tubulin through two cycles of polymerization-depolymerization in a high-molarity buffer: Protein Expr Purif, v. 32, p. 83-8.

Coureux, P. D., A. L. Wells, J. Ménétrey, C. M. Yengo, C. A. Morris, H. L. Sweeney, and A. Houdusse, 2003, A structural state of the myosin V motor without bound nucleotide: Nature, v. 425, p. 419-23.

Desai, A., and T. J. Mitchison, 1998, Preparation and characterization of caged fluorescein tubulin: Methods Enzymol, v. 298, p. 125-32.

Endow, S. A., S. J. Kang, L. L. Satterwhite, M. D. Rose, V. P. Skeen, and E. D.

Salmon, 1994, Yeast Kar3 is a minus-end microtubule motor protein that destabilizes microtubules preferentially at the minus ends: EMBO J, v. 13, p. 2708-13.

Gigant, B., W. Wang, B. Dreier, Q. Jiang, L. Pecqueur, A. Plückthun, C. Wang, and M. Knossow, 2013, Structure of a kinesin-tubulin complex and implications for kinesin motility: Nat Struct Mol Biol, v. 20, p. 1001-1007.

Hirokawa, N., R. Nitta, and Y. Okada, 2009a, The mechanisms of kinesin motor motility: lessons from the monomeric motor KIF1A: Nat Rev Mol Cell Biol, v. 10, p. 877-84.

Hirokawa, N., Y. Noda, Y. Tanaka, and S. Niwa, 2009b, Kinesin superfamily motor proteins and intracellular transport: Nat Rev Mol Cell Biol, v. 10, p. 682-96.

Hirose, K., E. Akimaru, T. Akiba, S. A. Endow, and L. A. Amos, 2006, Large conformational changes in a kinesin motor catalyzed by interaction with microtubules: Mol Cell, v. 23, p. 913-23.

Hyman, A. A., S. Salser, D. N. Drechsel, N. Unwin, and T. J. Mitchison, 1992, Role of GTP hydrolysis in microtubule dynamics: information from a slowly hydrolyzable analogue, GMPCPP: Mol Biol Cell, v. 3, p. 1155-67.

Jacobson, C., B. Schnapp, and G. A. Banker, 2006, A change in the selective translocation of the Kinesin-1 motor domain marks the initial specification of the axon: Neuron, v. 49, p. 797-804.

Kikkawa, M., and N. Hirokawa, 2006, High-resolution cryo-EM maps show the nucleotide binding pocket of KIF1A in open and closed conformations: EMBO J, v. 25, p. 4187-94.

Kikkawa, M., E. P. Sablin, Y. Okada, H. Yajima, R. J. Fletterick, and N. Hirokawa, 2001, Switch-based mechanism of kinesin motors: Nature, v. 411, p. 439-45.

Kozielski, F., S. Sack, A. Marx, M. Thormählen, E. Schönbrunn, V. Biou, A. Thompson, E. M. Mandelkow, and E. Mandelkow, 1997, The crystal structure of dimeric kinesin and implications for microtubule-dependent motility: Cell, v. 91, p. 985-94.

Kull, F. J., E. P. Sablin, R. Lau, R. J. Fletterick, and R. D. Vale, 1996, Crystal structure of the kinesin motor domain reveals a structural similarity to myosin: Nature, v. 380, p. 550-5.

Löwe, J., H. Li, K. H. Downing, and E. Nogales, 2001, Refined structure of alpha

beta-tubulin at 3.5 A resolution: J Mol Biol, v. 313, p. 1045-57.

Morikawa, M., H. Yajima, R. Nitta, S. Inoue, T. Ogura, C. Sato, and N. Hirokawa, 2015, X-ray and Cryo-EM structures reveal mutual conformational changes of Kinesin and GTP-state microtubules upon binding: EMBO J, v. 34, p. 1270-86.

Nakata, T., and N. Hirokawa, 2003, Microtubules provide directional cues for polarized axonal transport through interaction with kinesin motor head: J Cell Biol, v. 162, p. 1045-55.

Nakata, T., S. Niwa, Y. Okada, F. Perez, and N. Hirokawa, 2011, Preferential binding of a kinesin-1 motor to GTP-tubulin-rich microtubules underlies polarized vesicle transport: J Cell Biol, v. 194, p. 245-55.

Nitta, R., M. Kikkawa, Y. Okada, and N. Hirokawa, 2004, KIF1A alternately uses two loops to bind microtubules: Science, v. 305, p. 678-83.

Nitta, R., Y. Okada, and N. Hirokawa, 2008, Structural model for strain-dependent microtubule activation of Mg-ADP release from kinesin: Nat Struct Mol Biol, v. 15, p. 1067-75.

Nogales, E., S. G. Wolf, and K. H. Downing, 1998, Structure of the alpha beta tubulin dimer by electron crystallography: Nature, v. 391, p. 199-203.

Ogura, T., and C. Sato, 2006, A fully automatic 3D reconstruction method using simulated annealing enables accurate posterioric angular assignment of protein projections: J Struct Biol, v. 156, p. 371-86.

Ogura, T., H. Yajima, R. Nitta, N. Hirokawa, and C. Sato, 2014, New simulated annealing approach considering helix bending applied to determine the 8.8Å structure of 15-protofilament microtubules: J Struct Biol.

Okada, Y., and N. Hirokawa, 1999, A processive single-headed motor: kinesin superfamily protein KIF1A: Science, v. 283, p. 1152-7.

Pettersen, E. F., T. D. Goddard, C. C. Huang, G. S. Couch, D. M. Greenblatt, E. C. Meng, and T. E. Ferrin, 2004, UCSF Chimera--a visualization system for exploratory research and analysis: J Comput Chem, v. 25, p. 1605-12.

Rice, S., A. W. Lin, D. Safer, C. L. Hart, N. Naber, B. O. Carragher, S. M. Cain, E. Pechatnikova, E. M. Wilson-Kubalek, M. Whittaker, E. Pate, R. Cooke, E. W. Taylor, R. A. Milligan, and R. D. Vale, 1999, A structural change in the kinesin motor protein that drives motility: Nature, v. 402, p. 778-84.

Sablin, E. P., R. B. Case, S. C. Dai, C. L. Hart, A. Ruby, R. D. Vale, and R. J. Fletterick, 1998, Direction determination in the minus-end-directed

kinesin motor ncd: Nature, v. 395, p. 813-6.

Sali, A., and T. L. Blundell, 1993, Comparative protein modelling by satisfaction of spatial restraints: J Mol Biol, v. 234, p. 779-815.

Shang, Z., K. Zhou, C. Xu, R. Csencsits, J. C. Cochran, and C. V. Sindelar, 2014, High-resolution structures of kinesin on microtubules provide a basis for nucleotide-gated force-generation: Elife, v. 3.

Sindelar, C. V., and K. H. Downing, 2007, The beginning of kinesin's force-generating cycle visualized at 9-A resolution: J Cell Biol, v. 177, p. 377-85.

Sindelar, C. V., and K. H. Downing, 2010, An atomic-level mechanism for activation of the kinesin molecular motors: Proc Natl Acad Sci U S A, v. 107, p. 4111-6.

Sweeney, H. L., and A. Houdusse, 2010, Structural and functional insights into the Myosin motor mechanism: Annu Rev Biophys, v. 39, p. 539-57.

Vale, R. D., C. M. Coppin, F. Malik, F. J. Kull, and R. A. Milligan, 1994, Tubulin GTP hydrolysis influences the structure, mechanical properties, and kinesin-driven transport of microtubules: J Biol Chem, v. 269, p. 23769-75.

Yajima, H., T. Ogura, R. Nitta, Y. Okada, C. Sato, and N. Hirokawa, 2012, Conformational changes in tubulin in GMPCPP and GDP-taxol microtubules observed by cryoelectron microscopy: J Cell Biol, v. 198, p. 315-22.

Yildiz, A., M. Tomishige, R. D. Vale, and P. R. Selvin, 2004, Kinesin walks hand-over-hand: Science, v. 303, p. 676-8.